

ON THE THEORY AND EXPERIMENTS OF TIME-REVERSAL
FOR SOURCE RECONSTRUCTION

by

Xiaoyao Feng

Submitted in partial fulfillment of the requirements
for the degree of Doctor of Philosophy

at

Dalhousie University
Halifax, Nova Scotia
August 2022

© Copyright by Xiaoyao Feng, 2022

*I dedicate this thesis to my early deceased mother for her devoting endless love
to my childhood in such a limited period,
and for telling her in heaven that I do live up to her expectations.*

TABLE OF CONTENTS

LIST OF TABLES	vi
LIST OF FIGURES	vii
ABSTRACT.....	x
LIST OF ABBREVIATIONS USED	xi
LIST OF SYMBOLS	xii
ACKNOWLEDGEMENTS.....	xiii
CHAPTER 1 INTRODUCTION	1
1.1 RESEARCH BACKGROUND.....	1
1.2 OBJECTIVES	6
1.3 ORGANIZATION	7
CHAPTER 2 FUNDAMENTALS OF TIME-REVERSAL (TR) METHODS	9
2.1 INTRODUCTION.....	9
2.2 THE ELECTROMAGNETIC FDTD MODEL AND ITS PROGRAMMING	9
2.3 FUNDAMENTALS OF THE ELECTROMAGNETIC TR.....	12
2.3.1 The TR in the Wave Physics	13
2.3.2 The TR in Electromagnetics	14
2.3.3 Electromagnetic TR Method in One Dimension	15
2.4 THE ISSUES PERTAINING TO THE TR METHOD	21
2.4.1 Spurious Sources.....	22
2.4.2 The TR Mirrors (TRM) Sensors	23
2.4.3 The TR with Discrete-Time Signal Processing.....	24
2.4.4 Simulations and Discussions.....	26
2.5 SUMMARY	27
CHAPTER 3 THE TR FOR SOURCE RECONSTRUCTION	29
3.1 INTRODUCTION.....	29

3.2 SOURCE RECONSTRUCTION	29
3.2.1 Electromagnetic Interference	30
3.2.2 Source Reconstruction	31
3.2.3 Problem Description of the TR Source Reconstruction.....	31
3.3 THE PROPOSED ADAPTIVE TR FOR SOURCE RECONSTRUCTION	32
3.3.1 The Adaptive TR Method	32
3.3.2 Simulations and Discussions.....	34
3.4 SUMMARY	36
CHAPTER 4 THE PROPOSED ENTROPY METHOD.....	37
4.1 INTRODUCTION.....	37
4.2 THE ENTROPY METHOD	37
4.2.1 Definition	37
4.2.2 “Bottom Noise”	40
4.3 THE THRESHOLD CRITERION.....	42
4.4 THE TR WITH ENTROPY	44
4.5 DISCUSSIONS AND LIMITATIONS	45
4.6 SUMMARY	46
CHAPTER 5 THE PROPOSED KURTOSIS METHOD.....	47
5.1 INTRODUCTION.....	47
5.2 DEFINITIONS	47
5.3 THE TR WITH SPACE KURTOSIS.....	48
5.4 THE TR WITH TIME KURTOSIS	51
5.5 SUMMARY	53
CHAPTER 6 EXPERIMENTAL VALIDATIONS	54
6.1 INTRODUCTION.....	54
6.2 THE TESTING EQUIPMENT	54
6.3 THE TR EXPERIMENTAL SETUP	56

6.3.1 The Algorithms for Handling Band-Limited Data.....	56
6.3.2 The Testing Diagram.....	57
6.3.3 Reciprocity.....	59
6.4 THE CONFORMAL FDTD MODELING	59
6.4.1 The Contour Path (CP) Method.....	59
6.4.2 The Sub-Gridding Technique.....	61
6.5 THE EXPERIMENTAL VALIDATION RESULTS	63
6.5.1 Experimental Hardware Setup.....	63
6.5.2 Experimental Results.....	65
6.5.3 Validations with Two Sensors.....	68
6.5.4 Discussions.....	70
6.6 SUMMARY.....	71
CHAPTER 7 CONCLUSION.....	73
7.1 CONCLUDING REMARKS.....	73
7.2 FUTURE WORK.....	74
BIBLIOGRAPHY.....	76
APPENDIX A THE FDTD PROGRAMMING DETAILS	87
APPENDIX B MATHEMATICAL PROPERTIES OF ENTROPY.....	91

LIST OF TABLES

Table 6.1	Positions of each port.....	64
-----------	-----------------------------	----

LIST OF FIGURES

Figure 2.1	Field components of a typical transverse electromagnetic (TEM) wave. (The dash line represents the TR non-causal and non-physical field).....	15
Figure 2.2	Electric field spatial distributions at different time steps. (a) $n = 350$. (b) $n = N_{\max}$	17
Figure 2.3	Magnetic field spatial distributions at different time steps. (a) $n = 350$. (b) $n = N_{\max}$	17
Figure 2.4	Electric and magnetic fields recorded at Probe-2. (a) Electric field. (b) Magnetic field.	18
Figure 2.5	The time-reversed signal of (2.14b) injected at Probe-2.....	19
Figure 2.6	Field distributions at the time step $m = 650$ in TR. (a) Electric field. (b) Magnetic field.	19
Figure 2.7	Electric field distributions in time and space of the TR process. (a) Temporal distribution at the grid $k_0 = 500$. (b) Spatial distribution at the time instant $m = 900$	20
Figure 2.8	Comparisons between the reconstructed source and the original source. (a) The reconstructed source. (b) The original source.	21
Figure 2.9	An example of electromagnetic field propagation in two dimensions; the dash lines indicate the directions of wave-propagation.	21
Figure 2.10	An example of spurious sources during the TR process.	22
Figure 2.11	The conventional TR reconstruction of an impulse line source with the FDTD method. (a) The original source excited at the initial time step ($n = 1$). (b) Normalized field distributions at the last time step ($n = N - 1$) in Phase 2. .	27
Figure 3.1	Block diagram of a typical interference path.	30
Figure 3.2	Diagram of the source reconstruction setup.....	32
Figure 3.3	The adaptive TR reconstruction of two impulse sources with the FDTD	

	method. (a) One source reconstructed at (16, 5). (b) Another source reconstructed at (19, 6).	35
Figure 4.1	Spatial distributions of normalized electric fields (E_z) at different time steps. (a) $n = 1000$. (b) $n = 4500$	38
Figure 4.2	Temporal distributions of electric fields (E_z) at different nodes. (a) (14, 17). (b) (19, 6).	39
Figure 4.3	Computed entropy during the forward simulation.	40
Figure 4.4	Computed entropy in Phase 2.	41
Figure 4.5	The relationship between the entropy and E_n	43
Figure 4.6	The computed entropy in Phase 2.	44
Figure 4.7	The TR reconstruction of the source at $n = 9200$. (a) The reconstructed source at (23, 19). (b) The first original source.	45
Figure 4.8	The TR reconstruction of the source at $n = 8000$. (a) The reconstructed source at (6, 5). (b) The second original source.	45
Figure 4.9	Two sample field distributions with the same entropy. (a) Lower peak distribution. (b) Higher peak distribution.	46
Figure 5.1	The relationship between the space kurtosis and E_n	49
Figure 5.2	Temporal distributions of space kurtosis in Phase 2. (a) The computed space kurtosis versus time. (b) The zoomed-in space kurtosis computed between the 6000 th and 10000 th time steps.	50
Figure 5.3	The relationship between the time kurtosis and E_n	51
Figure 5.4	Spatial distributions of time kurtosis in Phase 2.	52
Figure 6.1	Typical antennas. (a) Dipole antenna. (b) Loop antenna.	55
Figure 6.2	The diagram of the test setup.	58
Figure 6.3	Typical Yee's lattices. (a) Electric loop. (b) Magnetic loop.	60

Figure 6.4	The thin wire model.	62
Figure 6.5	The physical dimensions of the cavity developed.	63
Figure 6.6	The photo of the cavity.	64
Figure 6.7	2.92mm female connector with the probe antenna. (a) Structure and parameters. (b) Photo of the probe antenna.	65
Figure 6.8	Photo of the hardware setup and measurement.....	66
Figure 6.9	Screenshot of the CST simulation model.....	66
Figure 6.10	The time-reversed signal that is injected into the cavity.....	67
Figure 6.11	Electric field distributions with field concentration. (a) $x = 130\text{mm}$ plane. (b) $y = 74\text{mm}$ plane.....	67
Figure 6.12	The TR results with only one TRM (Port 3). (a) Time-reversed signal. (b) TR source reconstruction results.....	68
Figure 6.13	Time-reversed signal obtained from S_{62}	69
Figure 6.14	The TR field distribution results with two sensors. (a) $x = 30\text{mm}$ plane. (b) $y = 30\text{mm}$ plane.	69
Figure 6.15	The time-reversed signal (5-10 GHz) that is injected into the CST model...	70
Figure 6.16	Electric field distributions when the concentration occurs. (a) $x = 130\text{mm}$ plane. (b) $y = 74\text{mm}$ plane.	71

ABSTRACT

Time-reversal (TR) method has been attractive and effective in solving inverse problems due to its relative simplicity. It has been widely researched in acoustics, optics, communications, and electromagnetics. One of its applications is source reconstruction, where the electromagnetic TR method can replace expensive measurements and signal computations. However, much work has been confined to theoretical discussions and numerical simulations; there are still unresolved ambiguities and controversies about the TR method. They restrict further realistic applications of the TR method in the areas such as electromagnetic compatibility (EMC). Therefore, more extensive research on theories, algorithms, simulations and experimentations of the TR method is needed.

In this thesis, we start with the fundamental laws in wave physics and electromagnetics and present a new theoretical perspective of the TR method. We use the finite-difference time-domain (FDTD) method to conduct numerical studies and verifications. The results show that the TR method in a cavity can efficiently locate field concentrations and recover the sources. We discuss the limitations of the conventional TR method and subsequently propose a new adaptive method with the introduction and incorporation of entropy and kurtoses. We apply the newly proposed method to locate sources and compare it with the conventional methods. Numerical examples demonstrate the effectiveness and capabilities of the proposed method in source reconstruction.

Finally, we develop a hardware experiment and validate TR as a robust and straightforward method for source reconstruction. Since the testing equipment has a limited working bandwidth, we propose the processing algorithms to deal with the band-limited testing data. The algorithms can produce causal time-domain signals from the band-limited data that can be used for realistic TR source reconstruction. As a result, the TR method can be applied with practical measurements to recover source excitation time instants and locations. In other words, the methods and techniques proposed in this thesis pave the way for extensions and applications of the TR to complex and realistic problems.

LIST OF ABBREVIATIONS USED

PDE	Partial Differential Equation 1
CEM	Computational Electromagnetics 1
FDTD	Finite-Difference Time-Domain 2
TR	Time-Reversal 2
MRI	Magnetic Resonance Imaging 2
MIMO	Multiple-Input and Multiple-Output 3
DORT	Time-Reversal Operator Decomposition 4
MUSIC	Multiple Signal Classification 4
EMI	Electromagnetic Interference 5
EMC	Electromagnetic Compatibility 5
SNR	Signal-to-Noise Ratio 5
TRM	Time-Reversal Mirrors22
PEC	Perfect Electric Conducting23
RF	Radio Frequency54
VNA	Vector Network Analyzer55
IFT	Inverse Fourier Transform56
CP	Contour Path59

LIST OF SYMBOLS

E, H	electromagnetic field intensity	9
D, B	electromagnetic flux density	9
J	current density	9
ρ	charge density	9
r	position vector	9
t	time variable	9
ε	permittivity of a medium	9
μ	permeability of a medium	9
x, y, z	Cartesian coordinate variables	10
i, j, k	discrete coordinate variables	10
n, m	discrete time variable	10
δ	space increment of a spatial grid	10
Δt	time increment of a temporal grid	10
ψ	wave function	13
v	wave velocity	13
τ	shifted reversal of time	13
S	Poynting vector	14
q	source/input port	24
p	sensor/output port	24
$x[n]$	excitation signal	24
$\delta[n]$	Kronecker Delta function	24
$y[n]$	output/recorded signal	25
$h[n]$	impulse response	25
$s[n]$	TR reconstructed signal	25
L	total number of samples in space	38
N	total number of samples in time	38
α	entropy	38
E_n	random field strength	42
A	entropy threshold	43
β_s	space kurtosis	47
β_t	time kurtosis	47
B_s, B_t	kurtosis threshold	48
$S[k_f]$	scattering parameter	56
k_f	discrete sampling frequency	56

ACKNOWLEDGEMENTS

First, I would like to thank my supervisor Dr. Zhizhang David Chen, for his enthusiasm, patience, and guidance. His expertise impresses me, and I have learned a lot from him. His encouragement motivates me, especially in the difficult times of Covid-19 pandemics. Without his support and encouragement, I would not be able to finish my doctoral research phase on the TR source reconstruction and reach the goals of my research plan.

I would also thank my committee members, Dr. Sergey Ponomarenko and Dr. Guy Kember, for their critical comments and valuable suggestions on my research.

I would appreciate Dr. Jacek Ilow, Nicole Smith, Tamara Cantrill, Ola Hamada, and all the other ECED faculty and staff for their help and support in completing this thesis work.

My thanks also go to my collaborators Jun Cai and Juan Li from Fuzhou University for their cooperation in experimentations, and colleagues Mingyang Xia, Ge Xiao, and Dr. Junfeng Wang for their suggestions in the study and living at Dalhousie University.

Last but most importantly, I would like to thank my father for his advice and guidance since I was born. I am forever in debt and gratitude for his time, efforts, and energy in bringing me up and for his care about my career progression and growth.

CHAPTER 1 INTRODUCTION

1.1 RESEARCH BACKGROUND

Engineering problems are often modelled with partial differential equations (PDEs) such as the wave equation, diffusion equation, Laplace equation, and Maxwell's equations. Therefore, solving engineering problems often means solving these PDEs. There are mainly two ways of solving PDE, analytical and numerical. The analytical approach is accurate and explicit; hence it is preferred whenever applicable. However, analytical methods are usually applicable only to a very limited number of problems when the shapes, boundaries, or other mathematical properties of a structure or solution domain are simple and regular. In other words, the analytical methods are often unavailable for most practical situations, leading to a small range of applications. With the rapid development of microelectronics and computer technology, the numerical approach or numerical methods become feasible and available in solving the PDEs that have not been solved before. Numerical methods are often pivotal in solving many engineering problems in recent decades.

The first step in a numerical method is to discretize a problem domain in space or time, transforming an original continuous PDE mathematical model into a discrete one. For example, by applying numerical approximations of the differential operators, PDE models are transformed into discrete algebraic equations in the discrete domains of space or time. These discrete equations are very suitable for solutions with computer languages and programming. The solutions of the discrete equations are expected to be approximating analytical solutions to the original continuous PDEs. When the above numerical process is applied to solve electromagnetic problems, it leads to a research branch called "computational electromagnetics (CEM)".

In CEM, different numerical approaches, such as finite difference methods, moments methods, and finite element methods, have been developed. They have attracted much attention in the past decades. Due to its algorithmic simplicity and flexibility, the finite-difference time-domain (FDTD) method is one of the most widely used time-domain numerical techniques for electromagnetic modelling and simulations [1]. Yee first introduced this method in obtaining solutions to Maxwell's curl equations directly on a space grid in the time-domain in 1966 [2]. It was further developed during the next few years by Taflove's team [3-5]. Since then, applications and research interests in this method have soared as millions of publications related to FDTD can now be found [1, 6, 7]. The application range of FDTD has been expanded over a broad spectrum [7].

Since the FDTD method is a proven effective method in solving electromagnetic problems in time, we choose it for the research topic of this thesis, the time-reversal (TR) source reconstruction, in a relatively easy way [8].

The TR method can be traced back to 1957 [11]. It has since been applied to solve inverse problems in various fields, such as acoustics [12-14] and communication systems [15]. For example, in clinical applications with microwave imaging, Kosmas and Rappaport conducted research for breast cancer detection [16-18]. They started from a two-dimensional model based on magnetic resonance imaging (MRI) data to examine the feasibility of TR [16]. They expanded their work to a more realistic three-dimensional model later [17]. They also proposed a matched-filter approach to solving signal-processing-related problems [18]. All their work used the FDTD method for TR computation.

The TR process is a two-step procedure: first, signals (or fields) emitted by sources propagate in a problem domain and are recorded at the pre-selected output locations within the domain; this first step can be called forward simulation or measurement. The second

step is the so-called backward simulation or TR computation: the recorded signals are reversed in time and re-injected at the pre-selected output locations into the solution domain. The fields then propagate in the domain and should form the concentrations at the original source locations that are then identified. This two-step procedure is called the TR method [19].

In a solution domain (or a wireless channel in communication terms), electromagnetic wave or signal propagation observes the following phenomena: transmission, reflection, scattering, and diffraction. Specifically, an electromagnetic wave can travel from a particular direction and is incident onto an object and then reflected or scattered by the object. The intensity of the reflected or scattered wave depends on the frequency, the incident angle, the field polarization direction of the electromagnetic wave, and the shapes and material compositions of the object. The wave may also bend around the obstacle [20], which is called diffraction. These phenomena cause signal multipath, leading to multiple copies of a field signal being received at one location at different time delays and most likely with the forms distorted from the originally transmitted signal. Such multipath can degrade the performance of a communication system. In digital communication, multipath-caused degradation includes inter-symbol interference and errors in identifying a bit as zero or one. However, recent studies show that the multipath can also be utilized to generate positive effects on communications and signal detections. For example, multiple-input and multiple-output (MIMO) antenna systems use multipath to provide an extra degree of freedom to improve the capacity of a two-way communication system [21-27].

The TR is another method that takes advantage of multipath effects. The multipath signals will superimpose constructively or concentrate or focus at the original source locations after re-injecting the time-reversed signals into the solution domain. The propagation of the time-reversed signal through an inhomogeneous medium creates a sharp focus around the source locations, which may also be considered signal autocorrelations [10].

From the frequency domain perspective, the TR process can be regarded as a phase-conjugation operation [28] that has been studied extensively in optics since the 1970s. The phase-conjugation was used to offset distortions by the medium and applied to monochromatic waves [29]. For example, Henty and Stancil used a single-frequency phase-conjugation method and focused energy around two targets separated by one-half wavelength [30, 31]. Later, Fink and his collaborators designed a successful experiment showing TR focusing in the time domain with a broadband ultrasonic signal. They claimed that if there are several reflectors in the medium, the TR method can be iterated to make the TR signal focus on the most reflective one [32]. Furthermore, the TR has been realized with ultrasonic waves [33-38] and applied in acoustics [39-46]. The underlying principles of TR have been studied through theoretical analysis [47-50] and numerical simulations [51-53].

The TR methods have also been applied to perform selective focusing on passive targets. It relies on the decomposition of the TR operator and is called the TR operator decomposition (DORT) method [37, 38, 54-59]. It requires that the targets are well resolved and that the number of targets, M , should not be more than the number of the elements of the detection antenna array, N ($M \leq N$). With this method, target positions can be identified through the singular vectors associated with non-zero singular values using the background Green's function.

It is also possible to image a medium through computational TR [60, 61]. For example, a method called TR multiple signal classification (MUSIC) was proposed by Devaney to image a medium for target localization [62-64]. It can estimate the locations of targets accurately even in the presence of multiple scattering between the scattering objects and the targets in the medium. The target scattering strengths were computed by a non-linear iterative algorithm [65]. Compared with the DORT method, TR MUSIC has no requirements for the resolution of targets and uses the zero singular vectors and values [63].

Since Fink's team's work on TR of electromagnetic waves [66], the TR methods have been employed in radar detection, two-way communications, geolocation [67], electromagnetic interference and compatibility (EMI/EMC), and other applications [68, 69] in electromagnetics and microwave engineering.

In Cepni's work [9], TR focusing is used to improve the detection performance of a radar system in a highly cluttered environment as well as to enhance the Signal-to-Noise Ratio (SNR) of a two-way communication scheme. It demonstrates the gains achieved by electromagnetic TR methods over conventional radar methods in focusing radar beams and detecting the targets in a highly cluttered environment. The TR focusing and nulling performances were measured in a controlled scattering medium, a complex laboratory environment, and a cavity with rich multipath effects. Based on the analytical scheme and simulation results, measurements were conducted. The results show that conventional radars with a matched filter worked well in the case of a single target in the solution domain. However, as the environment becomes more complicated, the performance of the matched filter detection deteriorates. On the contrary, the TR methods automatically match the radar filter to the channel with inside scatterers and can achieve field energy focusing around the target object in a highly scattered medium.

Zhu and Jiang proposed a target detection scheme based on two-dimensional FDTD TR [70]. They showed that the cluttered channel could be cancelled first through the TR nulling techniques using multiple antennas. After a target enters the medium, the TR energy focuses around the target causing a higher power return. This method is called the TR adaptive interference cancellation (TRAIC) and was studied further with experiments [71-73]. The TR schemes were realized and compared with various detection schemes. Using single antenna TR methods, Moura and Jin provided different detection algorithms [74]. Using the two-dimensional FDTD simulations, Yavuz and Teixeira showed electromagnetic TR focusing in random media and looked into polarization's impact on

focusing performances [75]. Liu and his collaborators employed a ray-tracing model to compute the background Green's function and achieved good focus at the target with electromagnetic TR imaging [76]. Sarabandi's team demonstrated TR focusing effects in a forest environment using a physics-based fractal tree model [77].

In the case of two-way communications, the idea is to use a TR filter for each user and convolve the incoming data streams with the proper filter, making the signal focus on the users' physical location. Using a TR filter during the data transmission from the base station, the channel dispersion can be removed, and a capacity-enhanced communication link can be obtained. The TR filter can also be used in space division multiple access algorithms to spatially differentiate the users [78-80].

Another important TR application is source reconstruction, which is critical in electronic system designs: locating radiation sources for EMI/EMC; such a source localization is usually difficult to conduct by direct testing and measurements. On the other hand, the TR methods are simple and robust. Without the need for explicit quantifications of the multipath effects, source locations are recovered through "backward propagation" of the time-reversed field signals of the forward simulations or measurements that are recorded at the pre-selected output locations. Fan et al. developed a method to make band-limited field signals applicable to the TR method. It extracted the time domain signals feasible for use with the TR method from the band-limited field signals through simple expansions [19, 81-83]. Liang conducted research on the three-dimensional FDTD TR to diagnose faulty antenna elements [84]. However, most research on the topic has been confined to numerical simulations, and there are challenges and issues that still need to be addressed for practical applications. This thesis is intended to address these problems as elaborated in the following sections and chapters.

1.2 OBJECTIVES

The thesis aims to provide theoretical explanations and experimental validations of the TR method for source reconstruction. Although some work on the TR for source localization has been done so far, there are still unresolved ambiguities and application limitations about the TR method. More specifically, this thesis has the following four objectives.

The first objective is to review the FDTD method and the TR process and present and summarize the computing algorithms that can realize the conventional TR algorithm.

The second objective is to discuss and study the theory of the TR method and explain different phenomena in the TR-associated numerical experiments.

The third objective is to identify and formulate source reconstruction problems that are TR applicable in real-world applications and propose the techniques to execute the TR method effectively.

The last objective is to validate the TR method with actual hardware experiments and lay the groundwork for further TR applications in EMC and structure synthesis.

1.3 ORGANIZATION

The thesis is organized as follows:

In Chapter 2, we first introduce the FDTD method for solving electromagnetic problems. Then we analyze the electromagnetic TR method in the one-dimensional case; we discuss its advantages and deal with its limitations. Finally, we use numerical examples to demonstrate the limits of the conventional TR method.

In Chapter 3, we propose an adaptive TR method to overcome the conventional TR method's limitations and applied to the source reconstruction problem. To get a better TR performance, we introduce the entropy and electromagnetic kurtosis methods into the TR

method and enable the realistic applications of the TR method in Chapter 4 and Chapter 5.

In Chapter 6, we conduct hardware experiments to validate the TR method. Since the measurement data are band-limited frequency-domain data, we propose special processing algorithms to convert the measured frequency-domain data into time-domain data usable with the TR source reconstruction.

In Chapter 7, conclusions are made, and future topics for research and engineering are introduced. The publications as a result of this thesis work are listed in the Bibliography.

CHAPTER 2 FUNDAMENTALS OF TIME-REVERSAL (TR)

METHODS

2.1 INTRODUCTION

Since a TR method needs a numerical technique for its computation, we will first present a discrete electromagnetic model of the FDTD method. Then we introduce the TR method to electromagnetics. Finally, we apply the FDTD method to the TR process and carry out the TR process numerically.

Maxwell's time-dependent equations govern the time-varying electromagnetic fields in a linear and isotropic medium. They are:

$$\begin{cases} \nabla \times \mathbf{E}(\mathbf{r}, t) = -\frac{\partial \mathbf{B}(\mathbf{r}, t)}{\partial t} \\ \nabla \times \mathbf{H}(\mathbf{r}, t) = \frac{\partial \mathbf{D}(\mathbf{r}, t)}{\partial t} + \mathbf{J}(\mathbf{r}, t), \\ \nabla \cdot \mathbf{D}(\mathbf{r}, t) = \rho(\mathbf{r}, t) \\ \nabla \cdot \mathbf{B}(\mathbf{r}, t) = 0 \end{cases} \quad (2.1a)$$

$$\nabla \cdot \mathbf{J}(\mathbf{r}, t) = -\frac{\partial \rho(\mathbf{r}, t)}{\partial t}. \quad (2.1b)$$

$\mathbf{E}(\mathbf{r}, t)$ is the electric field intensity, $\mathbf{D}(\mathbf{r}, t)$ is the electric flux density, $\mathbf{H}(\mathbf{r}, t)$ is the magnetic field intensity, $\mathbf{B}(\mathbf{r}, t)$ is the magnetic flux density, $\mathbf{J}(\mathbf{r}, t)$ is the current density, and $\rho(\mathbf{r}, t)$ is the charge density. \mathbf{r} is the position vector and t is the time variable. The material constitutive relationship is $\mathbf{D}(\mathbf{r}, t) = \varepsilon \mathbf{E}(\mathbf{r}, t)$ with ε being the permittivity of the medium and $\mathbf{B}(\mathbf{r}, t) = \mu \mathbf{H}(\mathbf{r}, t)$ with μ being the permeability of the medium.

2.2 THE ELECTROMAGNETIC FDTD MODEL AND ITS PROGRAMMING

In the Cartesian coordinate system, Maxwell's time-dependent curl equations of (2.1) can

be written as:

$$\nabla \times \mathbf{E}(x, y, z, t) = -\mu(x, y, z) \frac{\partial \mathbf{H}(x, y, z, t)}{\partial t}, \quad (2.2a)$$

$$\nabla \times \mathbf{H}(x, y, z, t) = +\varepsilon(x, y, z) \frac{\partial \mathbf{E}(x, y, z, t)}{\partial t} + \mathbf{J}(x, y, z, t). \quad (2.2b)$$

The scalar form of (2.2) is a system of six PDEs:

$$\frac{\partial H_x}{\partial t} = \frac{1}{\mu} \left(\frac{\partial E_y}{\partial z} - \frac{\partial E_z}{\partial y} \right), \quad (2.3a)$$

$$\frac{\partial H_y}{\partial t} = \frac{1}{\mu} \left(\frac{\partial E_z}{\partial x} - \frac{\partial E_x}{\partial z} \right), \quad (2.3b)$$

$$\frac{\partial H_z}{\partial t} = \frac{1}{\mu} \left(\frac{\partial E_x}{\partial y} - \frac{\partial E_y}{\partial x} \right), \quad (2.3c)$$

$$\frac{\partial E_x}{\partial t} = \frac{1}{\varepsilon} \left(\frac{\partial H_z}{\partial y} - \frac{\partial H_y}{\partial z} - J_x \right), \quad (2.3d)$$

$$\frac{\partial E_y}{\partial t} = \frac{1}{\varepsilon} \left(\frac{\partial H_x}{\partial z} - \frac{\partial H_z}{\partial x} - J_y \right), \quad (2.3e)$$

$$\frac{\partial E_z}{\partial t} = \frac{1}{\varepsilon} \left(\frac{\partial H_y}{\partial x} - \frac{\partial H_x}{\partial y} - J_z \right). \quad (2.3f)$$

To solve the above equations numerically, we discretize the associated space-time solution domain with a spatial and temporal grid of δ being the space increment and Δt being the time increment. We denote any scalar component of electric (or magnetic) field at the position $(x_i = i\delta, y_j = j\delta, z_k = k\delta)$ and at the time instant $t = n\Delta t$ as $E(i, j, k, n)$ (or $H(i, j, k, n)$), where i, j, k , and n are integers. By approximating the derivatives in (2.3) with their

central finite difference approximations that are second-order accurate, the six PDEs of (2.3) are transformed into six discrete algebraic equations below [85]:

$$H_x(i, j + \frac{1}{2}, k + \frac{1}{2}, n + \frac{1}{2}) = H_x(i, j + \frac{1}{2}, k + \frac{1}{2}, n - \frac{1}{2}) + \frac{\Delta t}{\mu\delta} \left[E_y(i, j + \frac{1}{2}, k + 1, n) - E_y(i, j + \frac{1}{2}, k, n) + E_z(i, j, k + \frac{1}{2}, n) - E_z(i, j + 1, k + \frac{1}{2}, n) \right], \quad (2.4a)$$

$$H_y(i + \frac{1}{2}, j, k + \frac{1}{2}, n + \frac{1}{2}) = H_y(i + \frac{1}{2}, j, k + \frac{1}{2}, n - \frac{1}{2}) + \frac{\Delta t}{\mu\delta} \left[E_z(i + 1, j, k + \frac{1}{2}, n) - E_z(i, j, k + \frac{1}{2}, n) + E_x(i + \frac{1}{2}, j, k, n) - E_x(i + \frac{1}{2}, j, k + 1, n) \right], \quad (2.4b)$$

$$H_z(i + \frac{1}{2}, j + \frac{1}{2}, k, n + \frac{1}{2}) = H_z(i + \frac{1}{2}, j + \frac{1}{2}, k, n - \frac{1}{2}) + \frac{\Delta t}{\mu\delta} \left[E_x(i + \frac{1}{2}, j + 1, k, n) - E_x(i + \frac{1}{2}, j, k, n) + E_y(i, j + \frac{1}{2}, k, n) - E_y(i + 1, j + \frac{1}{2}, k, n) \right], \quad (2.4c)$$

$$E_x(i + \frac{1}{2}, j, k, n + 1) = E_x(i + \frac{1}{2}, j, k, n) + \frac{\Delta t}{\varepsilon\delta} \left[H_z(i + \frac{1}{2}, j + \frac{1}{2}, k, n + \frac{1}{2}) - H_z(i + \frac{1}{2}, j - \frac{1}{2}, k, n + \frac{1}{2}) + H_y(i + \frac{1}{2}, j, k - \frac{1}{2}, n + \frac{1}{2}) - H_y(i + \frac{1}{2}, j, k + \frac{1}{2}, n + \frac{1}{2}) - \delta J_x(i + \frac{1}{2}, j, k, n) \right], \quad (2.4d)$$

$$E_y(i, j + \frac{1}{2}, k, n + 1) = E_y(i, j + \frac{1}{2}, k, n) + \frac{\Delta t}{\varepsilon\delta} \left[H_x(i, j + \frac{1}{2}, k + \frac{1}{2}, n + \frac{1}{2}) - H_x(i, j + \frac{1}{2}, k - \frac{1}{2}, n + \frac{1}{2}) + H_z(i - \frac{1}{2}, j + \frac{1}{2}, k, n + \frac{1}{2}) - H_z(i + \frac{1}{2}, j + \frac{1}{2}, k, n + \frac{1}{2}) - \delta J_y(i, j + \frac{1}{2}, k, n) \right], \quad (2.4e)$$

$$E_z(i, j, k + \frac{1}{2}, n + 1) = E_z(i, j, k + \frac{1}{2}, n) + \frac{\Delta t}{\varepsilon\delta} \left[H_y(i + \frac{1}{2}, j, k + \frac{1}{2}, n + \frac{1}{2}) - H_y(i - \frac{1}{2}, j, k + \frac{1}{2}, n + \frac{1}{2}) + H_x(i, j - \frac{1}{2}, k + \frac{1}{2}, n + \frac{1}{2}) - H_x(i, j + \frac{1}{2}, k + \frac{1}{2}, n + \frac{1}{2}) - \delta J_z(i, j, k + \frac{1}{2}, n) \right]. \quad (2.4f)$$

Equation (2.4) of the FDTD method represents a discrete system, while (2.3) of the real-world problem is a continuous system. The solutions to (2.4) are approximate solutions of (2.3). In other words, the FDTD solutions are the numerical approximating solutions to a real-world electromagnetic problem. To ensure the numerical solutions' accuracy and stability, some conditions and requirements need to be satisfied. One of them is the stability

condition:

$$\frac{u_{\max}\Delta t}{\delta} \leq \frac{1}{\sqrt{n_s}}, \quad (2.5)$$

where n_s is the number of space dimensions, u_{\max} is the maximum phase velocity of an electromagnetic plane wave in the medium. To ensure the accuracy and make the numerical dispersion errors negligible, δ should be small enough, usually smaller than 1/10 of the minimum wavelength.

In programming (2.4), we need to modify the space and time indices since most computer programming languages do not allow the fraction of 1/2 in the indices of the array elements. As a result, we develop the correspondences between indices of the components in (2.4) and those in the actual programming. The detailed correspondences and the programmed equations are presented in Appendix A. We use the developed FDTD programs or codes for our analysis and simulations.

2.3 FUNDAMENTALS OF THE ELECTROMAGNETIC TR

The reversal of time has stimulated our imagination throughout human history. While philosophers and scientists insist on exploring the nature of time and speculate on the circumstances under which it could possibly be reversed, it is generally accepted that the second law of thermodynamics is preventing us from reversing the flow of time on earth, at least in this expanding universe [86].

Although the idea of TR is hard to imagine and realize, researchers keep studying related techniques by utilizing the time-symmetrical property of specific physical laws, such as the wave equation, to solve various inverse problems. In this section, we will examine the fundamentals of TR by looking into some basic electromagnetic equations, show a one-dimensional example for verifications, and present discussions to provide a new theoretical

insight and understanding into the TR method.

2.3.1 The TR in the Wave Physics

As mentioned before, we first take a look at a typical wave equation:

$$\left(\nabla^2 - \frac{1}{v^2} \frac{\partial^2}{\partial t^2} \right) \psi(\mathbf{r}, t) = f(\mathbf{r}, t). \quad (2.6)$$

$\psi(\mathbf{r}, t)$ is a scalar function that usually refers to potential or any field component with position vector \mathbf{r} ($= x\mathbf{e}_x + y\mathbf{e}_y + z\mathbf{e}_z$) and time t ($t \geq 0$). $f(\mathbf{r}, t)$ is a source function, and v is the wave velocity.

If we substitute the time variable t by $t = T_0 - \tau$, we can find that the first and second time derivatives become:

$$\frac{\partial}{\partial t} = \frac{\partial}{\partial \tau} \frac{\partial \tau}{\partial t} = -\frac{\partial}{\partial \tau}, \quad (2.7a)$$

$$\frac{\partial^2}{\partial t^2} = \frac{\partial}{\partial t} \left(\frac{\partial}{\partial t} \right) = -\frac{\partial}{\partial \tau} \left(-\frac{\partial}{\partial \tau} \right) = \frac{\partial^2}{\partial \tau^2}. \quad (2.7b)$$

τ is the shifted reversal of time, where T_0 is the time duration for which the TR operation is conducted.

As a result, the wave equation (2.6) transforms to:

$$\left(\nabla^2 - \frac{1}{v^2} \frac{\partial^2}{\partial \tau^2} \right) \psi(\mathbf{r}, \tau) = f(\mathbf{r}, \tau). \quad (2.8)$$

We can see that Equation (2.8) is in the same form as (2.6); this means that if $\psi(\mathbf{r}, t)$ is one solution of the wave equation, $\psi(\mathbf{r}, \tau) = \psi(\mathbf{r}, T_0 - t)$ is also a solution which is the

so-called time symmetry. In other words, a solution of (2.6) with the positive time represents a forward-propagating wave, while its time-reversed solution of (2.8) is equivalent to a backward-propagating wave which acts similar to a backward-playing movie [9]. However, this backward propagation does not exist in the real physical world and is non-causal but can only be realized mathematically or computationally. Thus, the idea of TR here often refers to computational TR or passive TR [86]. Such a computational TR can be valuable since its non-physical solutions may contain information about a forward physical solution as its time-reversed copy mathematically.

2.3.2 The TR in Electromagnetics

In the TR in electromagnetics, we reverse the time in electromagnetic fields. Mathematically, we substitute $t = T_0 - \tau$ into (2.1) and get the time-reversed Maxwell's equations:

$$\begin{cases} \nabla \times \mathbf{E}(\mathbf{r}, \tau) = \frac{\partial \mathbf{B}(\mathbf{r}, \tau)}{\partial \tau} = -\frac{\partial [-\mathbf{B}(\mathbf{r}, \tau)]}{\partial \tau} \\ \nabla \times \mathbf{H}(\mathbf{r}, \tau) = -\frac{\partial \mathbf{D}(\mathbf{r}, \tau)}{\partial \tau} + \mathbf{J}(\mathbf{r}, \tau) \Leftrightarrow \nabla \times [-\mathbf{H}(\mathbf{r}, \tau)] = \frac{\partial \mathbf{D}(\mathbf{r}, \tau)}{\partial \tau} + [-\mathbf{J}(\mathbf{r}, \tau)], \\ \nabla \cdot \mathbf{D}(\mathbf{r}, \tau) = \rho(\mathbf{r}, \tau) \\ \nabla \cdot \mathbf{B}(\mathbf{r}, \tau) = 0 \end{cases} \quad (2.9a)$$

$$\nabla \cdot \mathbf{J}(\mathbf{r}, \tau) = \frac{\partial \rho(\mathbf{r}, \tau)}{\partial \tau} \Leftrightarrow \nabla \cdot [-\mathbf{J}(\mathbf{r}, \tau)] = -\frac{\partial \rho(\mathbf{r}, \tau)}{\partial \tau}. \quad (2.9b)$$

The time-reversed (2.9) are different from the original (2.1), which leads to different physical implications. As seen in Figure 2.1, while the Poynting vector $\mathbf{S}(\mathbf{r}, t) = \mathbf{E}(\mathbf{r}, t) \times \mathbf{H}(\mathbf{r}, t)$ of (2.1) represents a physically realizable forward-propagating right-handed electromagnetic field, $\mathbf{S}(\mathbf{r}, \tau) = \mathbf{E}(\mathbf{r}, \tau) \times \mathbf{H}(\mathbf{r}, \tau)$ of (2.9) represents a backward-propagating left-handed field that is non-causal and does not exist in the real world. Further studies of the left-handed field and double-negative metamaterials are not the topics of this thesis; relevant discussions can be referred to research in those areas [86, 87].

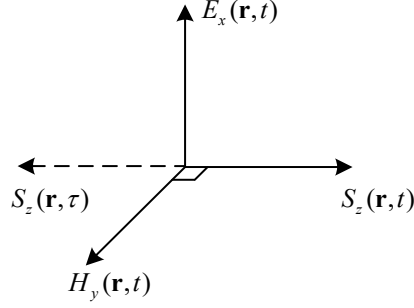


Figure 2.1 Field components of a typical transverse electromagnetic (TEM) wave. (The dash line represents the TR non-causal and non-physical field)

We can find that if $\mathbf{E}(\mathbf{r}, t)$, $\mathbf{D}(\mathbf{r}, t)$, $\rho(\mathbf{r}, t)$, $\mathbf{B}(\mathbf{r}, t)$, $\mathbf{H}(\mathbf{r}, t)$ and $\mathbf{J}(\mathbf{r}, t)$ are the solutions to an electromagnetic field of (2.1), $\mathbf{E}^{TR} = \mathbf{E}(\mathbf{r}, \tau)$, $\mathbf{D}^{TR} = \mathbf{D}(\mathbf{r}, \tau)$, $\rho^{TR} = \rho(\mathbf{r}, \tau)$, $\mathbf{B}^{TR} = -\mathbf{B}(\mathbf{r}, \tau)$, $\mathbf{H}^{TR} = -\mathbf{H}(\mathbf{r}, \tau)$ and $\mathbf{J}^{TR} = -\mathbf{J}(\mathbf{r}, \tau)$ are the physical solutions to (2.9), and they represent a TR electromagnetic field that propagates in the opposite direction. In other words, $\mathbf{S}^{TR} = \mathbf{E}^{TR} \times \mathbf{H}^{TR} = -\mathbf{E}(\mathbf{r}, \tau) \times \mathbf{H}(\mathbf{r}, \tau)$ is the TR field that we can apply to real problems. For simplicity, we show a one-dimensional electromagnetic propagation in the following sub-section to further illustrate this concept.

2.3.3 Electromagnetic TR Method in One Dimension

First, let us consider a one-dimensional plane wave propagating along the z -axis in free space with two non-zero field components, electric field E_x and magnetic field H_y . The two field components are dependent of z and t and independent of x and y . Maxwell's equations of (2.3) reduces to

$$\frac{\partial H_y}{\partial t} = -\frac{1}{\mu} \frac{\partial E_x}{\partial z}, \quad (2.10a)$$

$$\frac{\partial E_x}{\partial t} = -\frac{1}{\varepsilon} \left(\frac{\partial H_y}{\partial z} + J_x \right). \quad (2.10b)$$

The corresponding FDTD equations are:

$$H_y(k, n+1) = H_y(k, n) + \frac{\Delta t}{\mu \delta} [E_x(k, n) - E_x(k+1, n)], \quad (2.11a)$$

$$E_x(k+1, n+1) = E_x(k+1, n) + \frac{\Delta t}{\varepsilon \delta} [H_y(k, n) - H_y(k+1, n) - \delta J_x(k+1, n)]. \quad (2.11b)$$

The solution domain is free space. $\varepsilon = \varepsilon_0$, $\mu = \mu_0$, $\delta = c\Delta t$ with $c = 1/\sqrt{\mu_0\varepsilon_0}$ being the speed of light.

The lattice truncation boundary condition is used to absorb the field and avoid reflections at the boundaries of the solution domain:

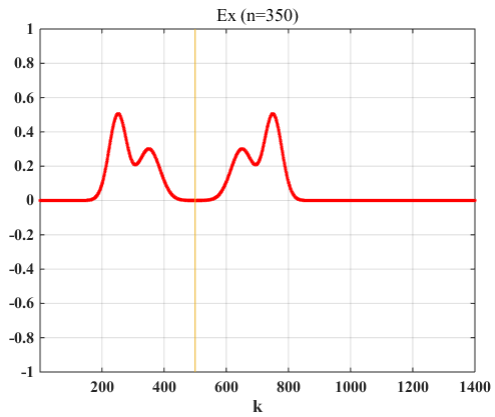
$$E_x(0, n+1) = E_x(1, n), \quad (2.12a)$$

$$E_x(K_{\max}, n+1) = E_x(K_{\max} - 1, n). \quad (2.12b)$$

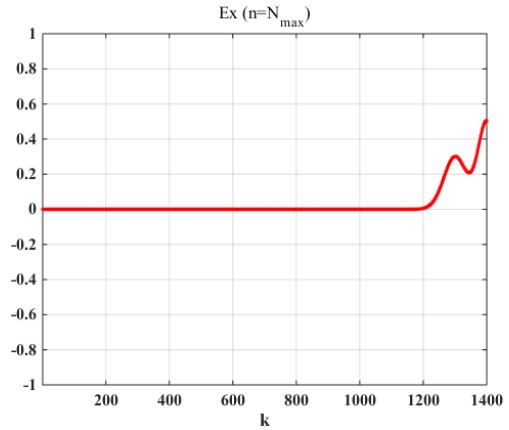
Now we put a source at the grid $k_0 = 500$, and two probes at $k_1 = 150$ (Probe-1) and $k_2 = 900$ (Probe-2). The source is a combination of two Gaussian functions; it has two peaks at $n = 100$ and 200 , respectively, and is programmed as follows:

$$E_x(k_0, n) = E_x(k_0, n) + \left[e^{-(n-100)^2/40^2} + 0.6e^{-(n-200)^2/50^2} \right]. \quad (2.13)$$

We run the simulation until the Gaussian waves have passed through the two probes, where a maximum time steps of $N_{\max} = 1000$ is chosen. The electric and magnetic field distributions at different time steps are shown below ($K_{\max} = 1400$):

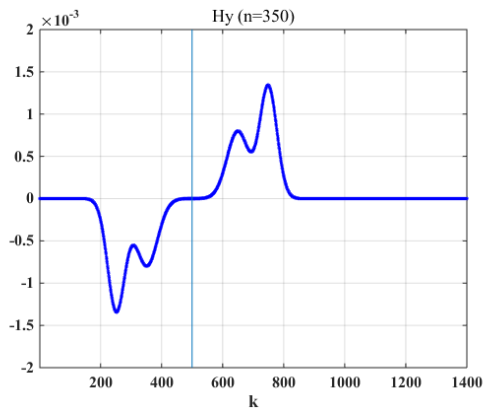


(a)

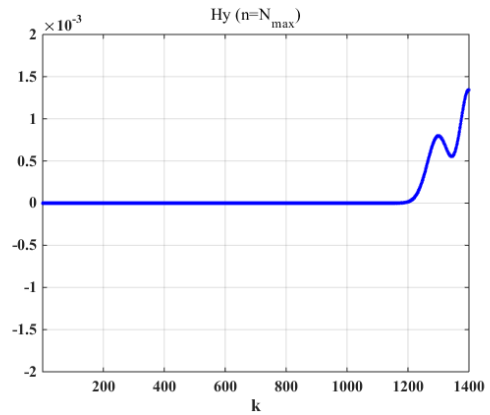


(b)

Figure 2.2 Electric field spatial distributions at different time steps. (a) $n = 350$. (b) $n = N_{\max}$.



(a)



(b)

Figure 2.3 Magnetic field spatial distributions at different time steps. (a) $n = 350$. (b) $n = N_{\max}$.

We can find that the source has generated two waves travelling in the positive or negative z -direction, respectively. The propagating waves are a combination of two Gaussian functions with peak values of 0.5 and 0.3, respectively. Figure 2.2(a) shows that the distributions of the electric field are spatially symmetric about the source location, while Figure 2.3(a) shows that magnetic field distributions are antisymmetric about the source

location; this agrees with the Poynting vectors of the two causal waves as they travel in two opposite directions. Figure 2.2(b) shows that the wave travelling in the negative z -direction reaches the end boundary and is absorbed. Figure 2.4 shows the field signal recorded at Probe-2.

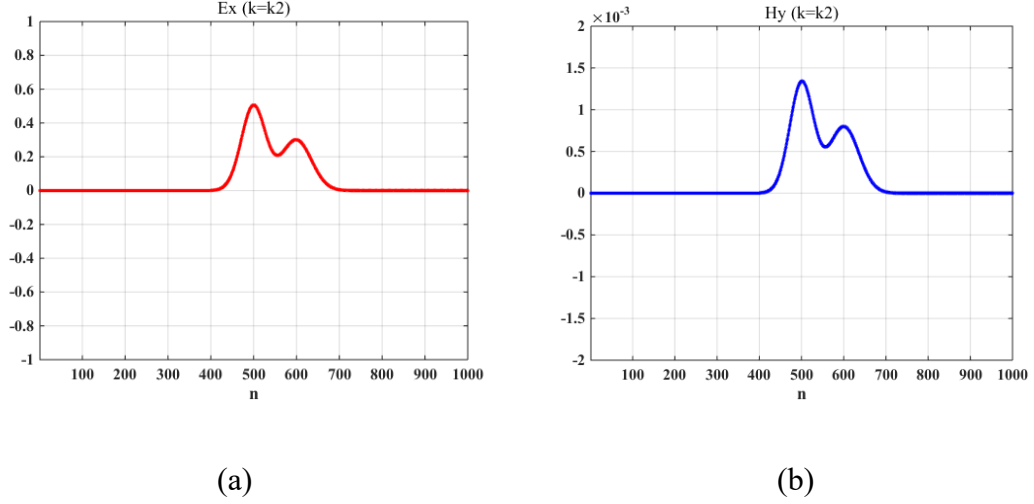


Figure 2.4 Electric and magnetic fields recorded at Probe-2. (a) Electric field. (b) Magnetic field.

After the forward propagation, we now time-reverse the electric fields received by the two probes to conduct a TR process:

$$E_x^{TR}(k_1, m) = E_x(k_1, N_{\max} - n), \quad (2.14a)$$

$$E_x^{TR}(k_2, m) = E_x(k_2, N_{\max} - n). \quad (2.14b)$$

where m is the time variable in TR process which we have introduced to distinguish it from n in the forward propagation.

They are injected into the one-dimensional domain at $k = k_1$ and $k = k_2$, respectively. Each of them excites two waves propagating in both $+z$ and $-z$ directions. Figure 2.5 shows the

time-reversed signal of (2.14b) that is injected at Probe-2. In Figure 2.6, the injected signal excites the waves travelling in the two directions with electric fields symmetric and magnetic fields antisymmetric about Probe-2 as expected. Similar observations can be made for the waves after the time-reversed signal of (2.14a) is injected at Probe-1.

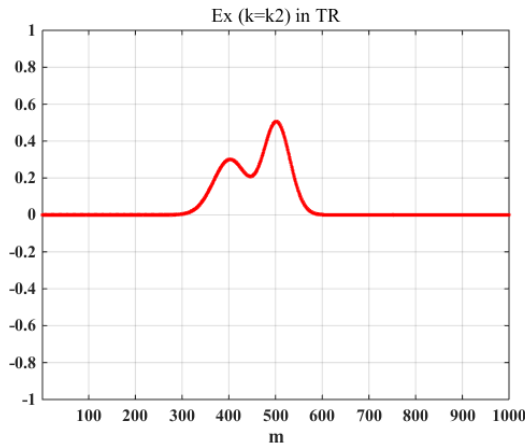
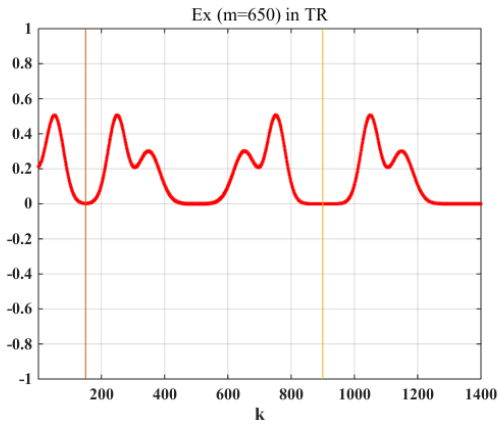
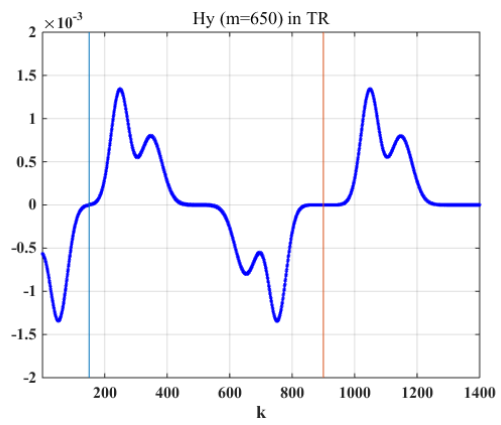


Figure 2.5 The time-reversed signal of (2.14b) injected at Probe-2.



(a)



(b)

Figure 2.6 Field distributions at the time step $m = 650$ in TR. (a) Electric field. (b) Magnetic field.

Finally, regardless of the waves travelling outside of the solution domain, the waves from the two probes travel and meet together during the TR process. Results are shown below:

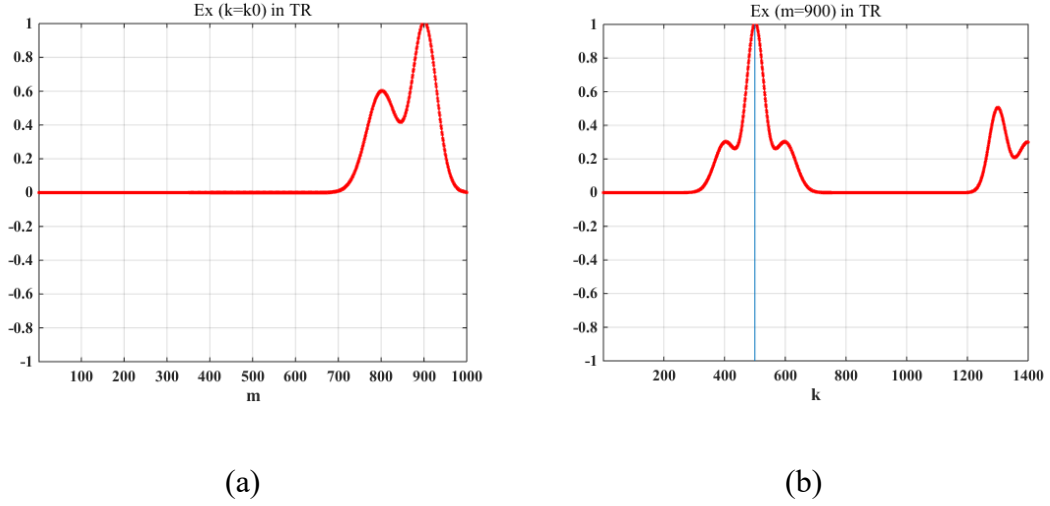


Figure 2.7 Electric field distributions in time and space of the TR process. (a) Temporal distribution at the grid $k_0 = 500$. (b) Spatial distribution at the time instant $m = 900$.

From Figure 2.7, a maximum amplitude of 1 is obtained at the time instant $m = 900$ and the grid $k_0 = 500$. This corresponds to the original source location and the peak in time also matches with the corresponding time step ($1000 - 900 = 100$) when the original source reaches its highest peak. With the results of Figure 2.7, we can reconstruct the original source from $E_x^{TR}(k_0, N_{\max} - m)$ and present it in Figure 2.8. Figure 2.8(a) is the reconstructed source, while Figure 2.8(b) is the original source; they match exactly.

The one-dimensional FDTD simulation confirms that the TR method allows us to reconstruct sources (the causes) from their emitted electromagnetic fields (the effects). In the following sections, we are to present further analysis of the method in higher dimensions.

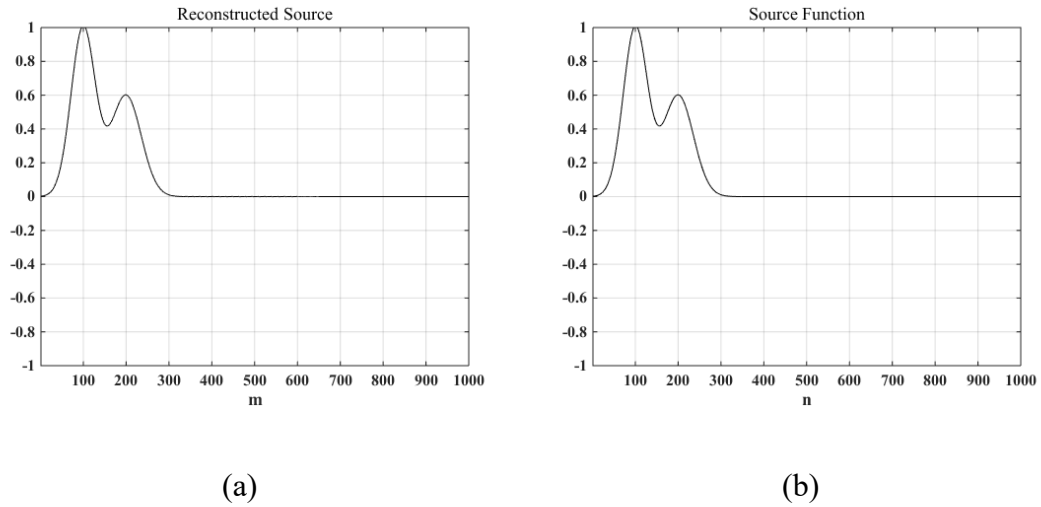


Figure 2.8 Comparisons between the reconstructed source and the original source. (a) The reconstructed source. (b) The original source.

2.4 THE ISSUES PERTAINING TO THE TR METHOD

In the last section, we have introduced TR in one dimension. We have mentioned that TR will also be applicable in higher-dimensional cases. Let us take a look at the two-dimensional case below:

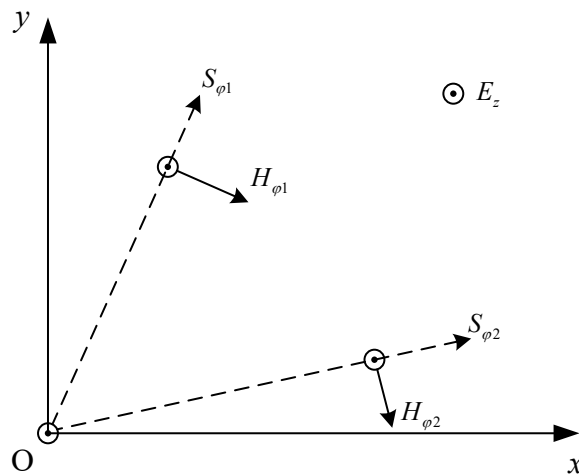


Figure 2.9 An example of electromagnetic field propagation in two dimensions; the dash lines indicate the directions of wave-propagation.

A TM-to-z wave is excited at the origin by an electric field; it will then propagate in all directions in the x - y plane, as illustrated in Figure 2.9. There are various issues with the TR method.

2.4.1 Spurious Sources

In the TR process, spurious sources may exist. Due to the symmetry in the problem domain (e.g., two probes used), if we can recover a source at the origin with TR, another spurious source may exist. Figure 2.10 shows that O' is another position other than the origin where two equal-phase surfaces intersect; in other words, the fields superimpose constructively not only at O but also at O' . The O' is then the spurious source point.

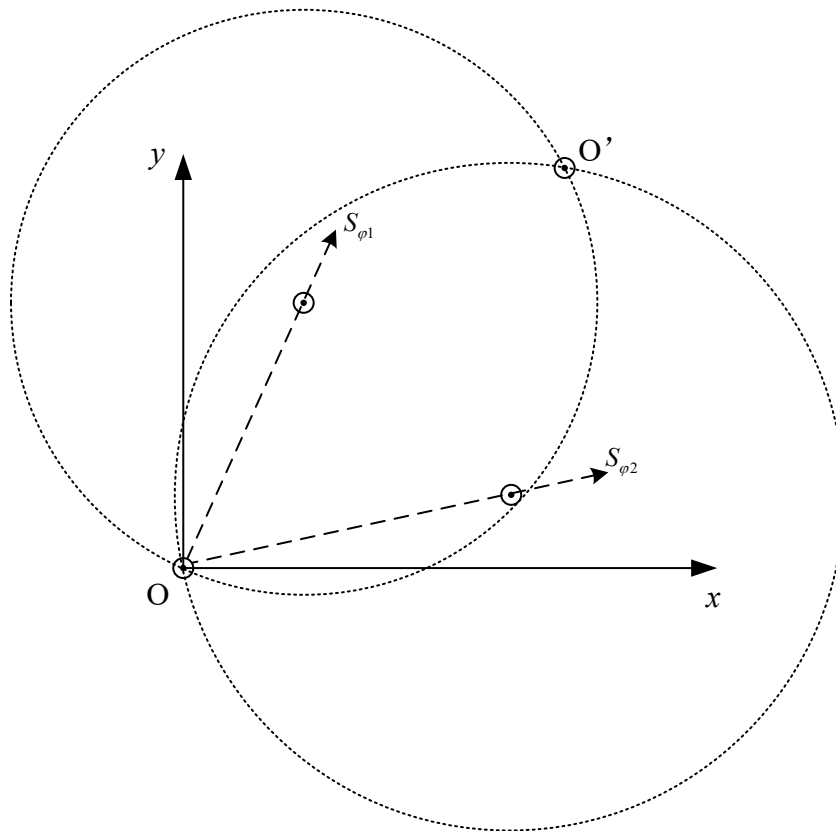


Figure 2.10 An example of spurious sources during the TR process.

To avoid spurious solutions, reasonable arrangements can be made in simulation and

experimentation. In particular, we should avoid having the field sensors in a straight line or use a non-symmetrical cavity to enclose the sources to be reconstructed.

2.4.2 The TR Mirrors (TRM) Sensors

Fink's team named electromagnetic TRM in 2010; it is the ensemble of an array of transceivers and electronics which can record, reverse and transmit signals [88].

In our example of Section 2.3.3, two TRM elements are used during the whole procedure. However, in two-dimensional or three-dimensional cases, only two elements cannot obtain all the information from the source. Such information or energy leakage may lead to false results or spurious sources. Only an infinite set of elements surrounding a source, which is called a completely closed TRM array [86], can fully recover the source without error [14]. However, of course, such an infinite set of elements is impossible to realize in the real world. As a result, information or energy leakage may lead to false or spurious solutions.

In practice, it is desirable in both computational and experimental scenarios to keep the number of TRM elements as small as possible without compromising the uniqueness and accuracy of the TR source reconstruction. This can indeed be achieved by performing the TR process in an air-filled cavity bounded by perfect electric conducting (PEC) walls. The PEC walls reflect electromagnetic waves back and forth, resulting in the ergodicity of the cavity; this means that all information emitted by the source will reach any other point in the cavity after some time. Such a cavity also confines the energy and enhances the TR effects with multipath. Consequently, we can use a single TRM element other than a closed array to recover the source with the possible highest resolution [86].

In a numerical simulation, the duration of the simulation (e.g., N_{\max}) or testing should be large enough to ensure that the travel distance of electromagnetic waves is much larger than the size of the cavity (e.g., 100 times) so that the waves travel uniformly and propagate

through almost all node locations. In such a way, the ergodicity condition is satisfied [86].

Considering the tradeoff between space and time, we usually use three TRM elements and place them arbitrarily in the solution domain. Since the cavity is ergodic, electromagnetic fields will pass through every location inside the cavity equally in a statistically averaged sense; thus, TRM locations will not affect the results of TR source reconstruction with the entropy or kurtoses, which will be discussed in Chapter 4 and Chapter 5 in details.

After discussing the above issues, we present the mathematical analysis of TR in signal processing as described in the sub-section below.

2.4.3 The TR with Discrete-Time Signal Processing

As described before, a conventional TR process can be summarized into two phases [84].

Phase 1: It is the forward simulation or measurement that records the field responses generated by unknown sources.

Phase 2: It is the backward simulation or TR computation that reconstructs the sources.

In Phase 1, we record the field responses for a certain period at arbitrarily preselected spatial TRM positions.

Suppose we have Q unknown impulse sources at Q different locations. We can express them as [83]

$$x_q[n] = a_q \delta[n], \quad q = 1, 2, \dots, Q. \quad (2.15)$$

a_q is the amplitude of the q^{th} impulse source. Note that (2.15) assumes that all the sources are excited at the same time step (or instant) $n = 0$.

The fields generated by the sources will propagate to the preselected TRM locations and are recorded there. Assume that we have P TRM elements. The field recorded at the p^{th} element can then be expressed as

$$y_p[n] = \sum_{q=1}^Q a_q h_{pq}[n], \quad p = 1, 2, \dots, P; n = 0, 1, \dots, N. \quad (2.16)$$

$h_{pq}[n]$ is the impulse response at the p^{th} element due to the impulse excitation at the unknown q^{th} source location. Here N is the total number of the time steps of the forward simulation or measurement.

Once the fields are recorded at the TRM locations, we complete Phase 1 and move to Phase 2.

In Phase 2, we time-reverse the received signal at the p^{th} TRM element, and it becomes

$$y_p^r[n] = y_p[N-n] = \sum_{q=1}^Q a_q h_{pq}[N-n]. \quad (2.17)$$

We re-inject the time-reversed signals into the solution domain at all the TRM elements and run the simulations. The TR signal recorded at the original q^{th} source location then becomes

$$\begin{aligned} s_q[n] &= \sum_{p=1}^P h_{qp}[n] \otimes y_p^r[n] = \sum_{p=1}^P \sum_{m=0}^n h_{qp}[m] y_p^r[n-m] \\ &= \sum_{p=1}^P \sum_{q'=1}^Q a_{q'} \sum_{m=0}^n h_{qp}[m] h_{p q'}[N-n+m] \end{aligned}, \quad (2.18)$$

where \otimes indicates discrete convolution.

At the last time step $n = N$, the TR signal $s_q[N]$ is

$$\begin{aligned}
s_q[N] &= \sum_{p=1}^P \sum_{q'=1}^Q a_{q'} \sum_{m=0}^N h_{pq}[m] h_{pq'}[m] \\
&= \sum_{p=1, q'=q'}^P a_q \left(\sum_{m=0}^N h_{pq}[m] h_{pq}[m] \right) + \sum_{p=1}^P \sum_{q'=1, q' \neq q}^Q a_{q'} \left(\sum_{m=0}^N h_{pq}[m] h_{pq'}[m] \right), \tag{2.19}
\end{aligned}$$

where $m = 0, 1, \dots, N$ is the dummy time index for the convolutional shift of time instants, q' is the index of source nodes which we have introduced to distinguish it from operations involving the index q , and $h_{qp}[n]$ equals $h_{pq}[n]$ in a reciprocal medium (see Section 6.3.3). The first term on the right-hand side of (2.19) may be recognized as the aggregation of the autocorrelation of $h_{pq}[n]$ and written as

$$R_{h_{pq}h_{pq}}[0] = \sum_{m=0}^N h_{pq}[m] h_{pq}[m] = \sum_{m=0}^N h_{pq}^2[m] \geq 0. \tag{2.20}$$

It is relatively larger than the second term on the right-hand side, which represents the summation of cross-correlation terms generated by different sources; this results in the field concentrations at the original Q source locations [83].

2.4.4 Simulations and Discussions

In our case here, we use FDTD simulations (to substitute the hardware experiment) for verifications. Figure 2.11 shows a three-dimensional example of the conventional TR process and its results.

As there is no ideal omnidirectional source exists, we place a TM-to- z line source at the center of a cubic cavity with $30 \times 30 \times 30$ cells. Three TRM elements are put at (13, 5, 3), (3, 19, 3) and (11, 7, 23) cells, respectively. The impulse line source excites at the 1st time step, and we carry on the forward simulation up to the 10000th time step (i.e., $N = 10000$).

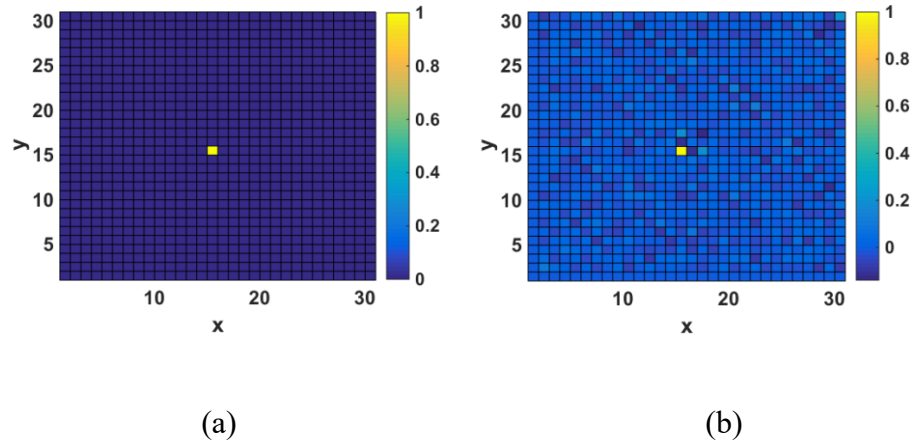


Figure 2.11 The conventional TR reconstruction of an impulse line source with the FDTD method. (a) The original source excited at the initial time step ($n = 1$). (b) Normalized field distributions at the last time step ($n = N - 1$) in Phase 2.

Note that in the above simulation, the source excites at $n = 1$; we identify the reconstructed source by the bright yellow cell in Figure 2.11(b) at $n = N - 1$ in Phase 2. However, unknown sources may excite at different unknown time instants rather than the same initial time in complex scenarios. The lack of this capability prevents the conventional TR from being applied to realistic problems. This issue is addressed in the next chapter.

2.5 SUMMARY

Together with relevant engineering applications and studies, the term TR has been proposed for decades so far; however, the lack of analysis about its mechanism and controversies in discussions impede the engineering realization of TR to a certain extent. Thus, TR is still a frontier in the area of inverse problems, which calls for new developments both in theory and practice.

In this chapter, based on previous studies on wave physics, we start with a simple one-dimensional example in electromagnetics and then analyze and demonstrate the fundamental theory of TR. To the best of the author's knowledge, the discussions and

analysis have not been reported in any literature so far. Finally, we discuss the method in a broader sense and verify the conventional TR with the introduced FDTD method. The conventional TR methods have limitations for real applications, and we will address them in the coming chapters.

CHAPTER 3 THE TR FOR SOURCE RECONSTRUCTION

3.1 INTRODUCTION

Despite recent years' progress, there are still major challenges and issues with the TR developed so far for practical applications. For example, source localization by peak identification may not work well in certain cases, especially when multiple sources exist, and relevant theory dealing with asynchronous sources has not been developed. Also, recovering signals or fields with frequency-domain measurements usually requires large computational and experimental resources. All these limitations motivate us for further developments of TR as one of the major applications of the FDTD method or time-domain numerical methods in general.

3.2 SOURCE RECONSTRUCTION

In this information era, the widespread application of electronic circuits and devices for automation, communication, computation and other purposes makes their operation in close spatial proximity to each other inevitable; they may then affect or interfere with each other adversely most of the time. Such interference has become a major concern for electronics engineers, and the situation will probably become even more severe in the near future because of three factors. First, the number uses of various electronic circuits and devices is growing rapidly. Second, thanks to the development of circuitry, more circuits are integrated into less space for convenience or other purposes. Third, clock frequencies have increased dramatically to over a gigahertz in recent decades. Therefore, today's engineers need to care beyond making their systems or devices function under ideal laboratory conditions. Products must be designed to "cooperate" with others nearby, and to comply with government regulations. Electronic systems or devices should neither be influenced by external electronic signals nor be a source of electronic noise that can pollute

their surrounding environment electromagnetically [89].

3.2.1 Electromagnetic Interference

When electronic or electrical systems in operation, they will produce electronic signals or electromagnetic emissions. In a broad sense, EMI covers a wide range of concerns: any electronic interference, electronic phenomenon, electronic signal or electromagnetic emission (including man-made and natural) that can cause undesirable or unacceptable response, malfunction, performance degradation, and which can be detected or located by the enemy prematurely is called EMI.

As engineers tend to focus on electromagnetic emission, it is worthy to point out that EMI contains two parts in general: emission and susceptibility. Electromagnetic susceptibility is of equal importance because of reciprocity to the emission.

Despite engineering problems, we are experiencing various EMI issues in our everyday life. For example, cellphones may interfere with radios, a working hair dryer may cause a mosaic television screen, and extreme weather conditions like lightning can destroy electrical circuits or devices. Possible interference paths vary for different systems, and problems; conductors, dielectrics, and air can all be the routes for electromagnetic energy transfer. Figure 3.1 shows the block diagram of a typical path.

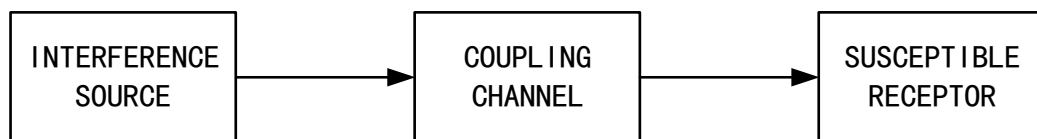


Figure 3.1 Block diagram of a typical interference path.

From the block diagram, a typical interference path is composed of an interference source, a coupling channel, and a susceptible receptor. The interference source is any entity, natural

phenomenon or environment that generates EMI. The susceptible receptor is the entity that reacts to EMI. The coupling channel is the medium where energy is transmitted through the interference source to the susceptible receptor. In theory, there are three approaches to dealing with a specific EMI problem concerning the three elements in Figure 3.1. One of them is to locate, reconstruct and then modify the interference sources.

3.2.2 Source Reconstruction

Identifying interference sources amounts to reconstructing the interference sources. However, source reconstruction is challenging since interference sources are generally hard to locate by direct measurements and testing.

Various methods have been developed for source reconstruction; however, most have limitations or serve specific purposes. For example, traditional maximum amplitude (MAM) and maximum energy methods (MEM) [90] only work in the case of a single source. Conventional passive indoor localization techniques such as time of arrival (TOA) and time-difference-of-arrival (TDOA) are susceptible to multipath effects; they need at least three observation points and generally work for tracking and locating in a relatively large setting such as rooms and buildings [91, 92]. Recently, it has been observed that electromagnetic TR methods cannot determine multiple asynchronous sources [67, 83, 93]. The magnitude or phase correlation criterion needs complex computations on the values of the Pearson correlation coefficient and only works for a single radiation source in an indoor environment [92]. Other frequency-domain source reconstruction methods require near-field scanning on a certain plane [94-96] or far-field measurement data on a hemisphere [97, 98], which increases the costs and complexity. All these challenges call for the development of new effective and efficient methods.

3.2.3 Problem Description of the TR Source Reconstruction

We perform our theoretical analysis of source reconstruction problems using the FDTD method. We place unknown (e.g., two) source(s) with several (e.g., three) sensor(s) or TRM elements inside a cavity. The unknown interference source(s) emits electromagnetic fields that propagate inside the cavity, and arrive at the sensors or TRM directly or indirectly through multiple reflections by the walls.

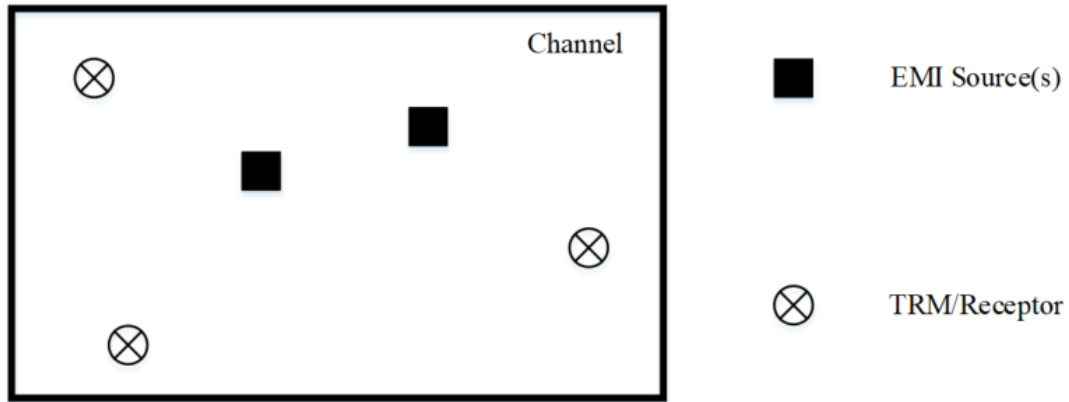


Figure 3.2 Diagram of the source reconstruction setup.

The interference source(s) is (are) like a black box; we usually know little about the source properties, including, but not limited to, locations, excitation time instants, band-width, and geometrical shapes. As we discussed in Section 2.4.4, the conventional TR can only recover the sources excited at the same initial time. To address the issue, we propose an adaptive TR method as described in the sections below.

3.3 THE PROPOSED ADAPTIVE TR FOR SOURCE RECONSTRUCTION

3.3.1 The Adaptive TR Method

In this subsection, we describe an adaptive TR method for extracting the asynchronous sources that exist in real-world scenarios. The method is still the two-phase approach: the first phase is the forward process that is the measurements of the field signals emitted by

the unknown sources, while the second phase is the TR of the signals measured in the first phase and re-injection of them into the problem domain (or the cavity in our case). In our experiments, for verification purposes, the first phase is normally replaced by the forward FDTD simulations, which are supposed to generate the same results as the measurement results. The mathematically quantitative descriptions of the TR method are presented as follows [99]:

In Phase 1, suppose that Q unknown asynchronous transient (impulse) sources $x_q[n]$ at Q locations are excited at different unknown time instants.

$$x_q[n] = a_q \delta[n - n_q], \quad q = 1, 2, \dots, Q. \quad (3.1)$$

Here a_q and n_q are the amplitude and the excitation time instant of the q^{th} source, respectively. $\delta[n]$ is Kronecker Delta function. Note that the sources can be asynchronous since n_q can be different.

Assume that we have P sensors or TRM elements that record the signals in the cavity, and the signal recorded at the p^{th} sensor or element can then be denoted as

$$y_p[n] = \sum_{q=1}^Q a_q h_{pq}[n - n_q], \quad p = 1, 2, \dots, P; n = 0, 1, \dots, N. \quad (3.2)$$

N is the number of time steps for which the simulation runs. $h_{pq}[n]$ is the impulse response at the p^{th} TRM element due to the impulse excitation at the q^{th} source location.

In Phase 2, the recorded signals are time-reversed and become

$$y_p^r[n] = y_p[N - n] = \sum_{q=1}^Q a_q h_{pq}[N - n + n_q]. \quad (3.3)$$

After the backward simulation executes for the same duration of N , the final output signal

at the original q th source location (or node) becomes

$$\begin{aligned}
s_q[n] &= \sum_{p=1}^P h_{qp}[n] \otimes y_p^r[n] = \sum_{p=1}^P \sum_{m=0}^n h_{qp}[m] y_p^r[n-m] \\
&= \sum_{p=1}^P \sum_{q'=1}^Q a_{q'} \sum_{m=0}^n h_{qp}[m] h_{pq'}[N-n+n_{q'}+m]
\end{aligned} \tag{3.4}$$

At $n = N - n_q$, the TR signal $s_q[n]$ is

$$\begin{aligned}
s_q[N-n_q] &= \sum_{p=1}^P \sum_{q'=1}^Q a_{q'} \sum_{m=0}^{N-n_q} h_{pq}[m] h_{pq'}[m] \\
&= \sum_{p=1, q'=q}^P a_q \left(\sum_{m=0}^{N-n_q} h_{pq}^2[m] \right) + \sum_{p=1}^P \sum_{q'=1, q' \neq q}^Q a_{q'} \left(\sum_{m=0}^{N-n_q} h_{pq}[m] h_{pq'}[m] \right)
\end{aligned} \tag{3.5}$$

Equation (3.5) has two terms: the first term is the autocorrelation term of $h_{pq}[n]$, which is always positive, and the second term is the cross-correlation term of different $h_{pq}[n]$. Since the autocorrelation term is relatively much larger than the cross-correlation term [83], the output signal intensity $s_q[N-n_q]$ is larger than the fields at any other non-source locations, contributing to field concentrations at the original Q sources locations, respectively. In other words, by observing the TR response of (3.4) in Phase 2, we should see the field concentrations at $n = N - n_q$ and can reconstruct the sources from there. These sources can be asynchronous since they are excited at different time instants $n = n_q$.

3.3.2 Simulations and Discussions

We conduct a numerical test below to check the feasibility of the above adaptive TR. For illustration purposes, we employ the two-dimensional simulations in the rest of this thesis without loss of generality.

Suppose we place two impulse sources in a two-dimensional cavity with 30×30 cells. Three TRM sensors are placed at (13, 5), (3, 19) and (11, 7) cell locations, respectively. The

impulse sources are excited at random locations and time instants generated by the random number generation function of Matlab. We simulate up to 10000th time step (i.e., $N = 10000$).

Because we are supposed to have no information about the sources' exact locations and excitation time, we have to save all the computed TR data in a large matrix of $30 \times 30 \times 10000$ elements. With the saved field distributions, we then search and find the two maximum electric field (E_z) values; the two electric sources with maximum amplitudes are reconstructed at different time steps, and are shown in Figure 3.3.

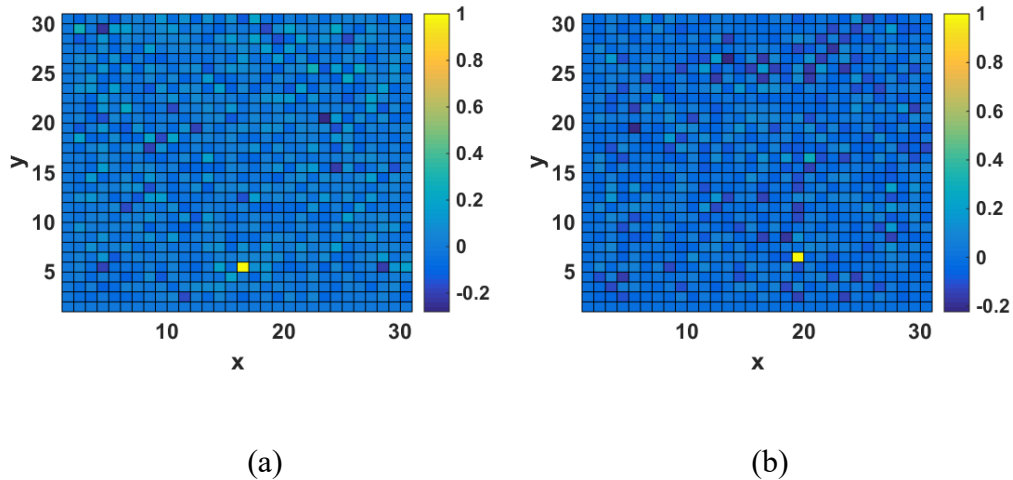


Figure 3.3 The adaptive TR reconstruction of two impulse sources with the FDTD method. (a) One source reconstructed at (16, 5). (b) Another source reconstructed at (19, 6).

For the example above, we are kind of knowing that two sources exist, so we pursue to identify two maximum values in the TR data. If we do not have this prior knowledge, searching the data and finding the field concentrations will be very challenging and sometimes exhausting for (1) the data of field distributions are significantly huge, and (2) field distributions can be quite random and hard to tell. Therefore, although the above adaptive TR is much more improved than the conventional TR in reconstructing the

asynchronous sources, we still need to find ways to reconstruct the sources automatically in an effective and efficient manner. To do so, we propose and develop the entropy and kurtosis methods as described in the next chapters.

3.4 SUMMARY

As conventional TR has limitations in application to real engineering problems, we propose the adaptive TR to overcome them. The newly proposed adaptive TR is capable of reconstructing multiple asynchronous sources. We conduct numerical experiments to verify our method, which lays the groundwork for further developments of TR in microwave theory and applications.

CHAPTER 4 THE PROPOSED ENTROPY METHOD

4.1 INTRODUCTION

The well-known term entropy comes from statistical physics. It is defined to measure the degree of disorder or randomness of a system.

Entropy has been developed to be a statistical quantity used in data processing so far. For example, it was applied to image processing with the inverse of the varimax criterion to restore star field images [100]. Later, it was employed to localize subsurface objects in remote sensing [101] and extended to the detection of breast cancers in MRI [16, 17]. Other applications include localization of dielectric structures [102], interference [93], and radar targets [103].

In image processing, the concept of entropy is used to detect the quality of an image [100]. The smaller the entropy is, the clearer the image is; it reflects the amount of average information statistically in an image and represents the aggregated features of the grayscale distribution of the image. We then find out that a visualized electromagnetic field distribution is analogous to an image: the better field patterns correspond to clearer images. Therefore, we can introduce the entropy measure into the TR process: at the time of the field concentration or focusing (similar to an image becoming clear), we will get small entropy of the field within a solution domain; at any other time of no field focusing, the field distributes randomly, and we will get relatively large entropy. In other words, entropy minima can be used to determine the time instants when the field focusing is formed (and therefore, the sources are reconstructed in Phase 2).

4.2 THE ENTROPY METHOD

4.2.1 Definition

We now consider time-varying electric (or magnetic) fields $E(i, j, k, n)$ (or $H(i, j, k, n)$) that are sampled at spatial positions ($x = i\delta, y = j\delta, z = k\delta$) and at time instants $t = n\Delta t$. Assume that the total number of samples in space is L and that in time is N , respectively. With the FDTD method, we introduce the entropy α in reference to its use in image processing as described below [100, 104]:

$$\alpha(n) = \frac{\left[\sum_i \sum_j \sum_k E^2(i, j, k, n) \right]^2}{\sum_i \sum_j \sum_k E^4(i, j, k, n)}. \quad (4.1)$$

It can be observed that entropy is a function of time step n . Let us take an example to see its feasibility in identifying excitation time instants of multiple sources.

Suppose we place two impulse sources in the same two-dimensional cavity. One impulse source is $x_1[n] = \delta[n - 1000]$ located at the node (14, 17) and the other is $x_2[n] = \delta[n - 4500]$ located at the node (19, 6). The total time steps used in this 30×30 -cell cavity is $N = 10000$.

Results of FDTD forward simulation are shown in Figure 4.1, 4.2 and 4.3.

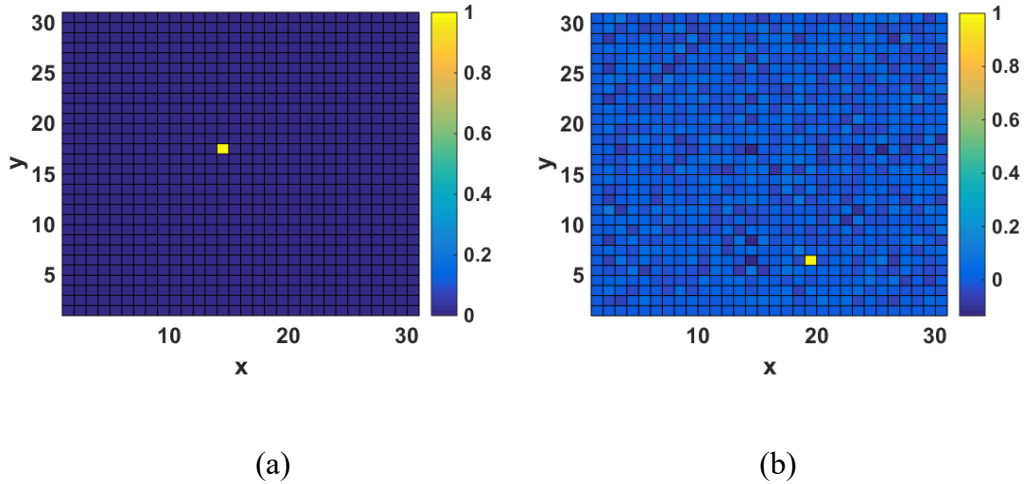
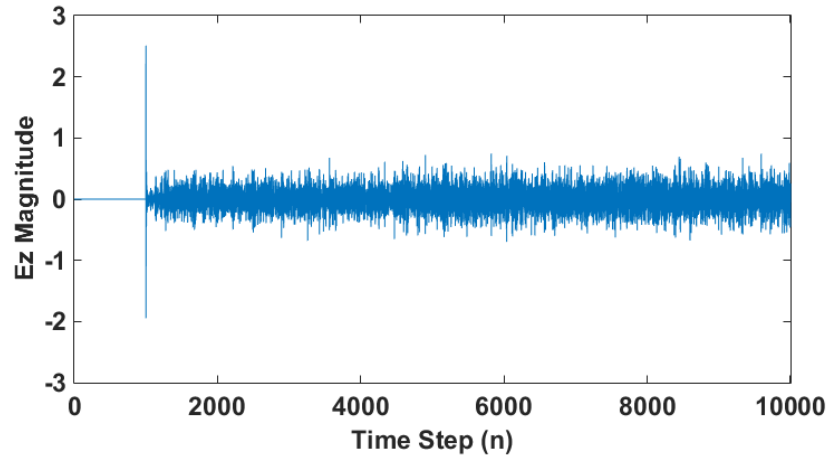
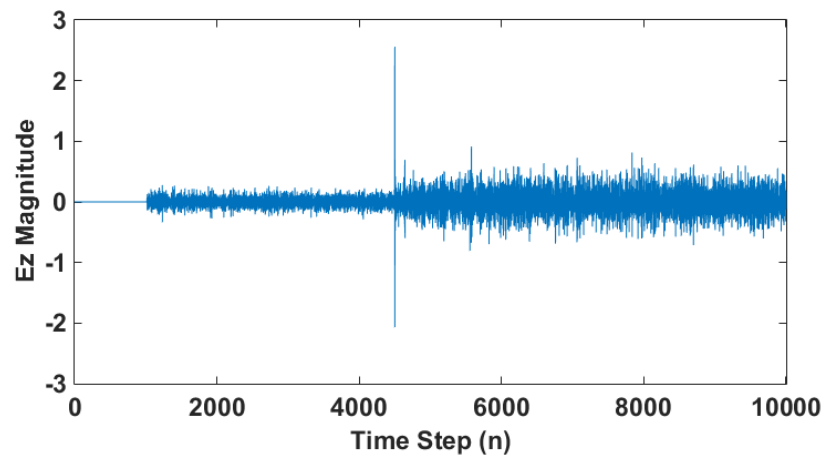


Figure 4.1 Spatial distributions of normalized electric fields (E_z) at different time steps. (a) $n = 1000$. (b) $n = 4500$.



(a)



(b)

Figure 4.2 Temporal distributions of electric fields (E_z) at different nodes. (a) (14, 17). (b) (19, 6).

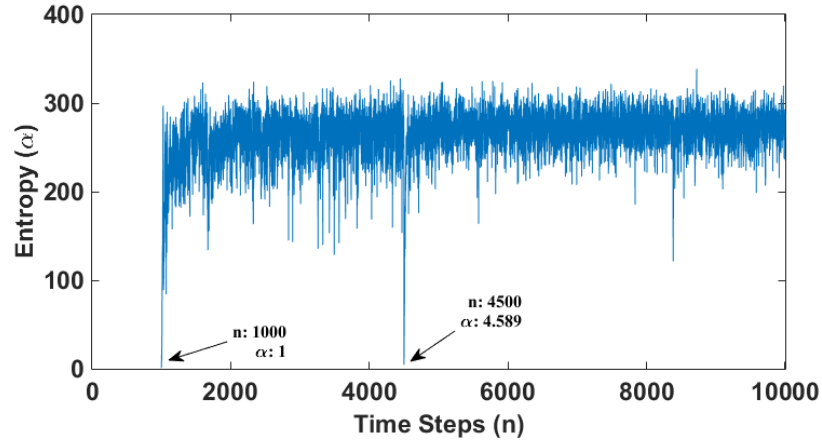


Figure 4.3 Computed entropy during the forward simulation.

Two impulse sources can be easily identified both in space and time in Figure 4.1 and Figure 4.2. From Figure 4.3, several local minima of entropy occur during the simulation. The first local minimum comes out at $n_1 = 1000$ time step, where $\alpha = 1$; this equals the theoretical lower limit of the defined entropy (see Appendix B). It means that before the 1000th time step, the electric field is not excited, and the entropy does not exist. After the 1000th time step, the electromagnetic fields propagate inside the cavity, and the entropy varies with time in relatively large values. Until the $n_2 = 4500$ time step, another local minimum with a relatively small value occurs, which means that another source is excited.

4.2.2 “Bottom Noise”

From Figure 4.3, we can also observe that some other local minima between 100 and 200 exist during the forward simulation (Phase 1 of TR); they do not match with any sources. However, it is hard to judge whether they correspond to any sources without prior knowledge, especially if it is further applied in Phase 2. We now compute the entropy value in Phase 2 and the results are shown in Figure 4.4.

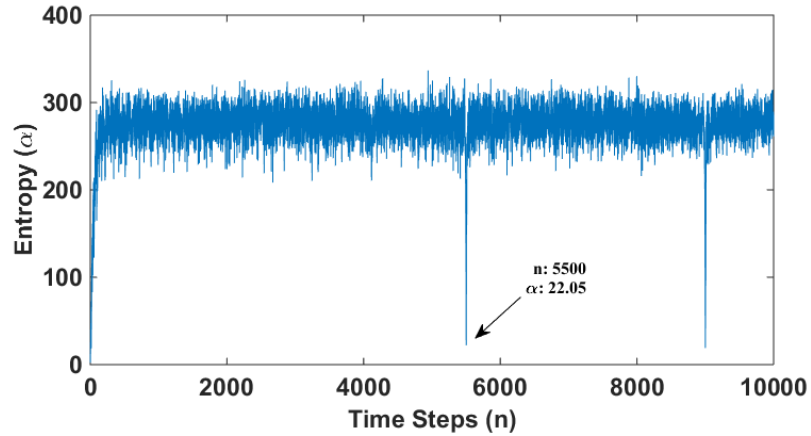


Figure 4.4 Computed entropy in Phase 2.

We can see that there are three apparent local minima here. The first one appears at the beginning as time-reversed signals are injected at TRM locations. The other two minima with values under 100 correspond to the time instants when two sources are excited and can be reconstructed.

The second minimum has $n = 5500$ and $\alpha = 22.05$. This entropy value is much higher than the corresponding entropy value of 4.589 in Phase 1 (or Figure 4.3); this is because TR cannot fully reconstruct the original amplitude due to the fact that there are only a limited number of TRM sensors that record the fields with finite emitted energy captured during Phase 1; such finite energy also spreads to other spatial locations of the cavity, and it creates more and less random field distributions, as discussed in Section 2.4.2. Despite the finite energy and its spread, it still concentrates during Phase 2 because of autocorrelations and presents the possibility of source reconstruction.

As shown in Figure 4.4, the energy spread during Phase 2 presents relatively higher entropy values and behaves like noise. Since this is not real noise, we will refer to it as entropy's “bottom noise” in the following discussions. Here “bottom” refers to the lower magnitude or power of the field signals compared to those of the sources.

The “bottom noise” contains quite a few local minima, in particular, in the range of 200 to 300 in entropy value. Then the question arises: how do we differentiate the minima that represent the real sources from those in the “bottom noise”? Our approach to solving the problem is to use a threshold. The threshold technique has been used in many areas. In the following section, we propose a way to determine the threshold.

4.3 THE THRESHOLD CRITERION

The entropy threshold is the value below which any entropy is considered correspondent to potential sources; the time instants at which the entropy local minima occur are considered the source-excitation time instants. Because of the cavity’s ergodicity, factors like locations and duration have little impact on entropy values and, therefore, on the threshold.

To determine the threshold value, we carry out the following computation. The entropy is computed on a distribution with a single unit impulse source located at one node and random fields distributed at the rest of the nodes. The random field distributions are used to present the possible variety of field distributions at different time instants; they are of uniformly distributed random values with a magnitude between $-E_n$ and E_n . We repeat the computation with different strengths of the random fields, and the results are shown in Figure 4.5 [105].

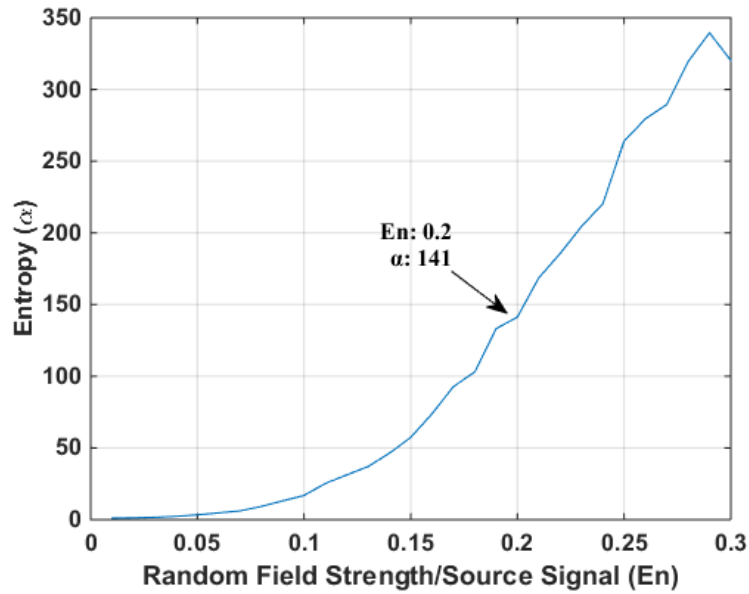


Figure 4.5 The relationship between the entropy and E_n .

Figure 4.5 shows the computed entropy versus the ratio of the random fields' strength to the single source strength. The ratio is denoted as E_n . As seen, when the ratio increases (i.e., stronger “bottom noise”), the entropy increases.

We take $E_n = 0.2$ as the threshold point as it amounts to that the maximum strength of the random field distributions is 20% of the source. We consider it as the breaking point between the valid entropy minima and the false minima. At $E_n = 0.2$, $\alpha = 141$. Therefore, $A(\alpha) = 141$ is used as the entropy threshold: any entropy value below it will be considered as the valid local entropy minima for source identifications.

Now the threshold can pick the potential peaks and be smaller than the “bottom noise”. It should be pointed out that even with the threshold found above, there may still be false identifications of the invalid local minima, which do not give the correct source excitation time instants. However, since we need to plot the field distributions at the identified time steps (or instants) to provide final confirmation of the field concentrations, we can remove the false results by examining the field distributions plotted.

4.4 THE TR WITH ENTROPY

After introducing the threshold criterion, we can now apply the entropy method to the sources reconstruction problem with TR.

Suppose we place two impulse sources in the cavity. One impulse is $x_1[n] = 0.92\delta[n - 800]$ located at the node (23, 19) and the other is $x_2[n] = 1.2\delta[n - 2000]$ located at the node (6, 5). Three TRM elements are located at (13, 5), (3, 19) and (11, 7) nodes, respectively. TR results are shown below.

From Figure 4.6, the red line is the threshold $A = 141$. Two local minima near the end of Phase 2 are smaller than the threshold, which indicates the time instants when sources are excited. Figure 4.7 and 4.8 show the reconstructed sources with bright yellow cells, which match the locations of the original sources.

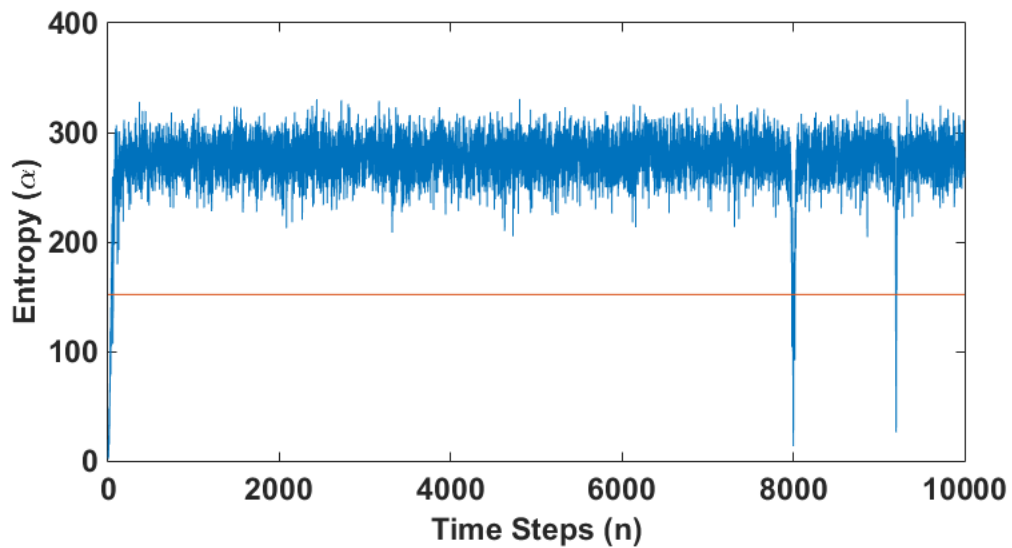


Figure 4.6 The computed entropy in Phase 2.

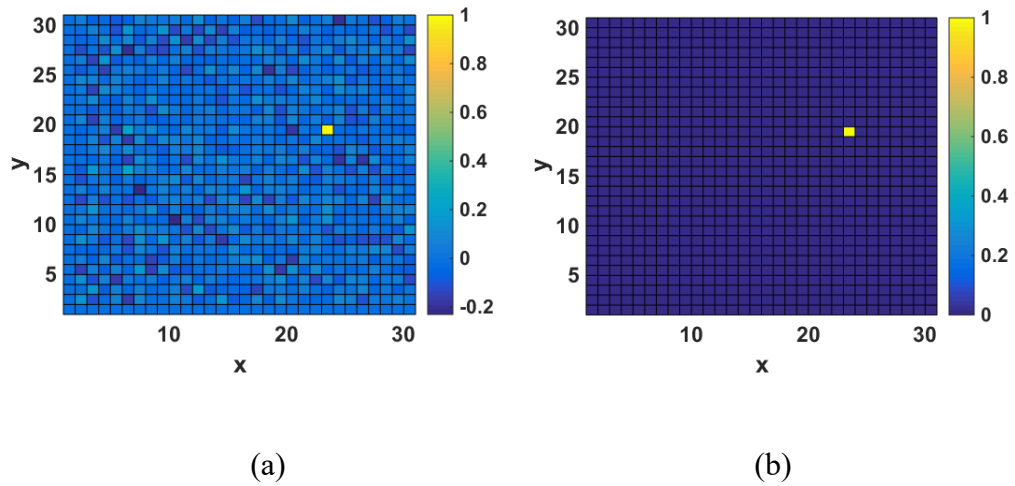


Figure 4.7 The TR reconstruction of the source at $n = 9200$. (a) The reconstructed source at (23, 19). (b) The first original source.

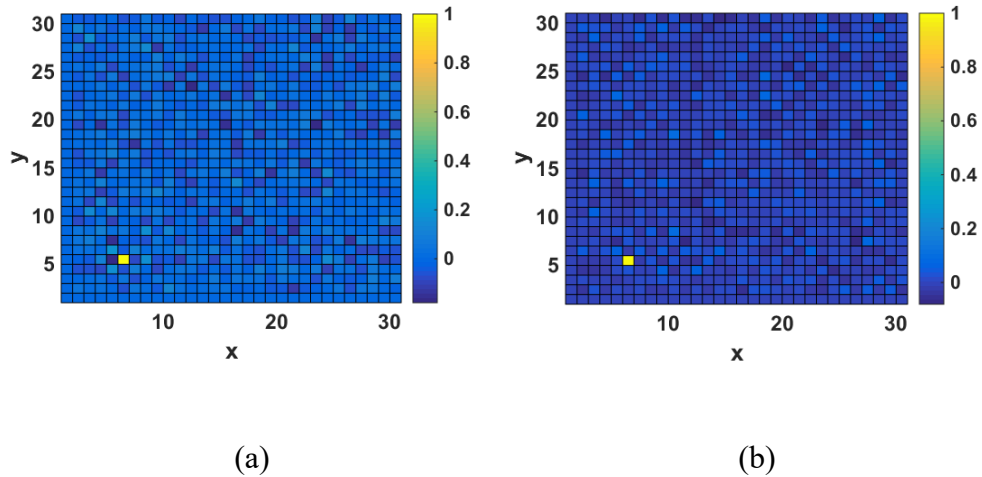


Figure 4.8 The TR reconstruction of the source at $n = 8000$. (a) The reconstructed source at (6, 5). (b) The second original source.

4.5 DISCUSSIONS AND LIMITATIONS

From the definition of entropy, we can find that entropy value may be not unique in certain cases. Let us make a comparison of two simple field distributions as follows:

0.3	0.3	0.3
0.3	1.0	0.3
0.3	0.3	0.3

(a)

-0.3	-0.3	-0.3
-0.3	1.0	-0.3
-0.3	-0.3	-0.3

(b)

Figure 4.9 Two sample field distributions with the same entropy. (a) Lower peak distribution. (b) Higher peak distribution.

It is clear that these two distributions have the same entropy. However, Figure 4.9(b) has a definitely higher peak, but entropy values cannot differentiate these two kinds of distributions with different averages. Thus, we introduce a progressive kurtosis method to make up for this shortcoming in the next chapter.

4.6 SUMMARY

In this chapter, we have introduced the entropy method to reconstruct multiple asynchronous sources. We have also introduced the threshold and one way to compute it. Consequently, the proposed entropy method can automatically find all possible field concentration time instants by identifying the local minima of entropy in Phase 2. After plotting the spatial distributions of fields at these time instants, source locations can also be reconstructed. In the next chapter, we propose another method, the progressive electromagnetic kurtosis method, to reconstruct the sources better.

CHAPTER 5 THE PROPOSED KURTOSIS METHOD

5.1 INTRODUCTION

Kurtosis is a concept often used in statistical data analysis which quantifies the proportion and “sharpness” of the outliers in a random variable distribution [106-108]: the larger the kurtosis value, the larger proportion and values of the outliers in a data set. Recent research has shown that the use of kurtosis can be not only in statistics but also in other fields like communication systems [109, 110] (and references therein).

Theoretically, the exact calculation of kurtosis requires a set of an infinite number of data. In reality, this is impossible. Therefore, different ways of estimating the kurtosis from a finite sampled data set have been proposed. One of them is sample kurtosis. It is a scaled version of the ratio between the fourth central moment and the square of the second central moment. Inspired by the above ideas, we introduced electromagnetic kurtosis and incorporated it into TR in this chapter.

5.2 DEFINITIONS

There are two types of electromagnetic kurtosis; with the same FDTD scheme in entropy definition, we define kurtoses as follows [99]:

$$\beta_s(n) = \frac{\frac{1}{L} \sum_i \sum_j \sum_k \{E(i, j, k, n) - \bar{E}(n)\}^4}{\left[\frac{1}{L} \sum_i \sum_j \sum_k \{E(i, j, k, n) - \bar{E}(n)\}^2 \right]^2}, \quad (5.1a)$$

$$\beta_t(i, j, k) = \frac{\frac{1}{N} \sum_n \{E(i, j, k, n) - \bar{E}(i, j, k)\}^4}{\left[\frac{1}{N} \sum_n \{E(i, j, k, n) - \bar{E}(i, j, k)\}^2 \right]^2}. \quad (5.1b)$$

L is the total number of cells in the space and N is the total number of the time steps.

In the first definition of (5.1a), $\bar{E}(n)$ is the field value averaged over all the FDTD grids in the spatial region at the time step n . Since the triple summation is taken with respect to all the spatial grids, we refer β_s as “space kurtosis”; it characterizes field distributions in space as its name suggests, and it is a function of the time step n .

In the second definition of (5.1b), $\bar{E}(i, j, k)$ is the field value averaged over all the FDTD time steps at the spatial node (i, j, k) , and the summation is taken with respect to all the time steps. Thus, we refer it as “time kurtosis”; β_t is a function of the spatial coordinates and can characterize the temporal distributions of fields (or signals).

Let us take the same example used for the entropy computation to verify the capability of space and time kurtoses in identifying source excitation time instants and locations, respectively. The first source is $x_1[n] = 0.92\delta[n - 800]$ at the node $(23, 19)$ and the second source is $x_2[n] = 1.2\delta[n - 2000]$ at the node $(6, 5)$.

5.3 THE TR WITH SPACE KURTOSIS

In examining (5.1a), the definition of space kurtosis is similar to entropy. Thus, it works like the entropy method in the TR for source reconstruction.

First, we establish the threshold of the space kurtosis by applying the approach similar to that for the entropy as described in the last chapter [105]. The result is shown in Figure 5.1, and we obtain the threshold $B_s(\beta_s) = 6.39$.

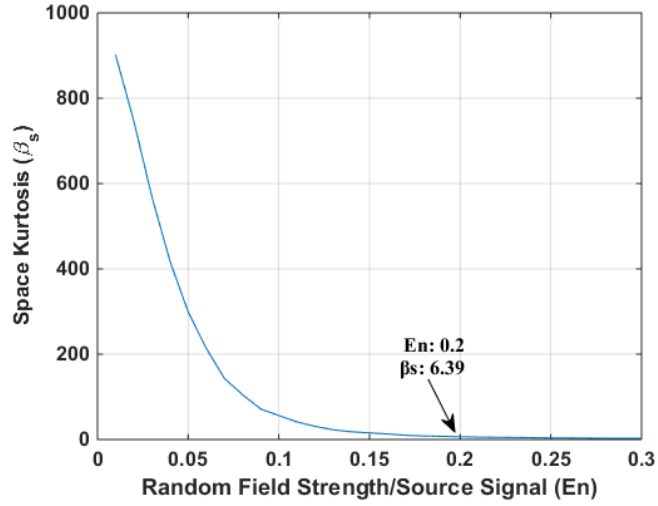
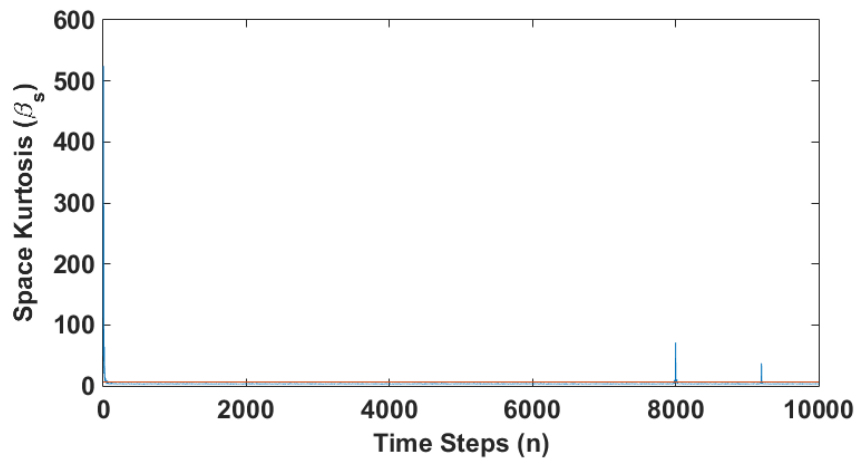


Figure 5.1 The relationship between the space kurtosis and E_n .

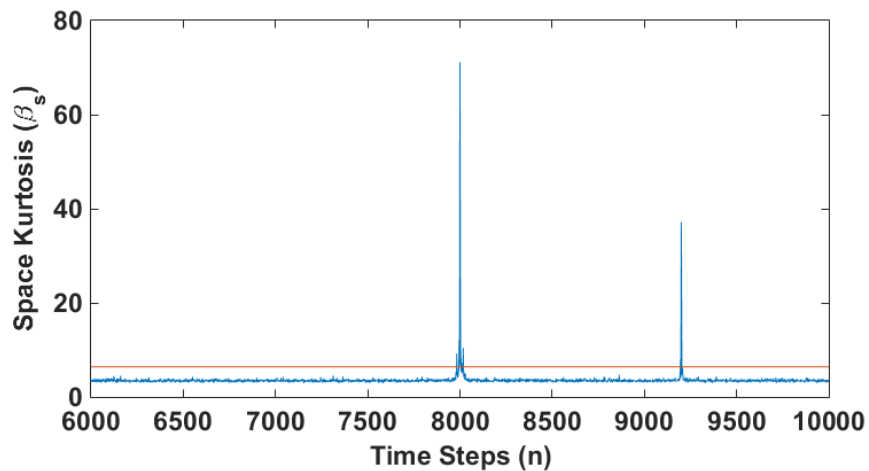
With the threshold obtained, we conduct the same TR experiment: one impulse source of $x_1[n] = 0.92\delta[n - 800]$ locates at the node (23, 19) and the other $x_2[n] = 1.2\delta[n - 2000]$ locates at the node (6, 5). The result is shown in Figure 5.2; the red line shows the threshold $B_s = 6.39$. The first maximum of space kurtosis exists at the beginning of Phase 2; it does not correspond to the original source but the time-reversed signals that are re-injected into the cavity (as the sources of Phase 2). Two local maxima near the end of Phase 2 which are bigger than the threshold indicate the time instants when original sources are excited. Finally, we can plot the field distributions at these time instants and localize the original sources, and the results are shown in Figure 4.7 and 4.8.

Again, it should be pointed out that even with the threshold, there may still be certain scenarios with false identifications of the invalid local maxima (e.g., two small spikes near the time step $n = 8000$). Since we need to plot the field distributions to provide final confirmation of the field concentrations, we can remove the false results by examining the field distributions plotted. On the other hand, kurtosis values of reconstructed sources are affected by various factors in the real world, and the threshold is a function of sources' amount, amplitudes and locations, testing duration, bandwidth and so on. Here we propose

one way to determine the threshold, but there is still enough space between the “bottom noise” and valid local maxima. Further study on other threshold criteria is much desired according to future application scenarios.



(a)



(b)

Figure 5.2 Temporal distributions of space kurtosis in Phase 2. (a) The computed space kurtosis versus time. (b) The zoomed-in space kurtosis computed between the 6000th and 10000th time steps.

The above TR process of source localization with space kurtosis can be summarized into two steps: First, we identify the time instants when space kurtosis reaches the valid local maxima in Phase 2 of the TR. Then we plot the associated field distributions at the time instants identified in Phase 2 and localize the sources.

5.4 THE TR WITH TIME KURTOSIS

Although the proposed space kurtosis can reconstruct source locations, the process requires the identification of excitation time instants first and then plotting the fields' spatial distributions in Phase 2. However, with the time kurtosis of (5.1b), sources can be directly reconstructed spatially.

First, we still need to obtain the threshold of time kurtosis. Considering the same scenario of previous configurations and employing an approach similar to that of obtaining the threshold of space kurtosis, we can get the threshold of $B_t(\beta_t) = 4.22$ [99].

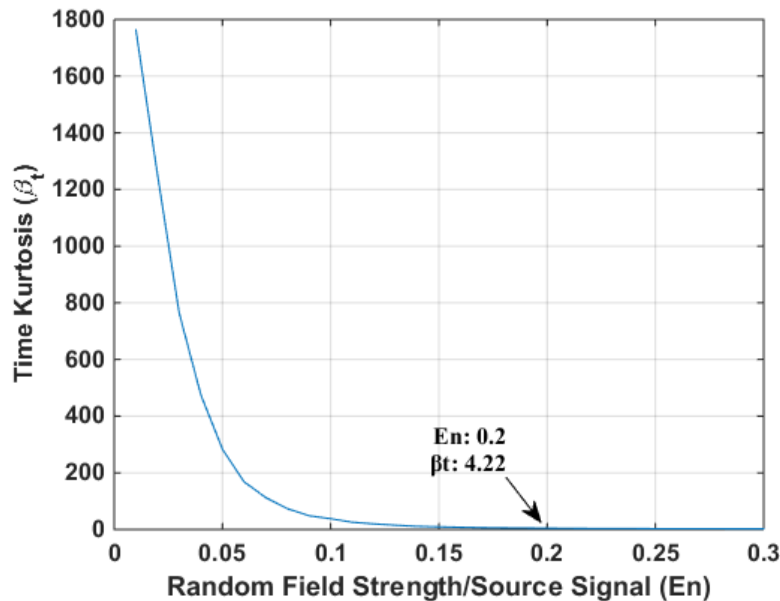


Figure 5.3 The relationship between the time kurtosis and E_n .

Then we conduct the TR computation of the same cavity configuration as for the space kurtosis. After computing the time kurtosis of (5.1b), the local maxima of two nodes are found to reach above the threshold: $\beta_t(23, 19) = 5.48$ and $\beta_t(6, 5) = 6.15$. These nodes correspond exactly to the locations of the two original sources. Figure 5.4 shows the spatial distributions of time kurtosis with bright cells matching with those original sources in Figure 4.7 and 4.8. The multiple asynchronous sources are localized successfully.

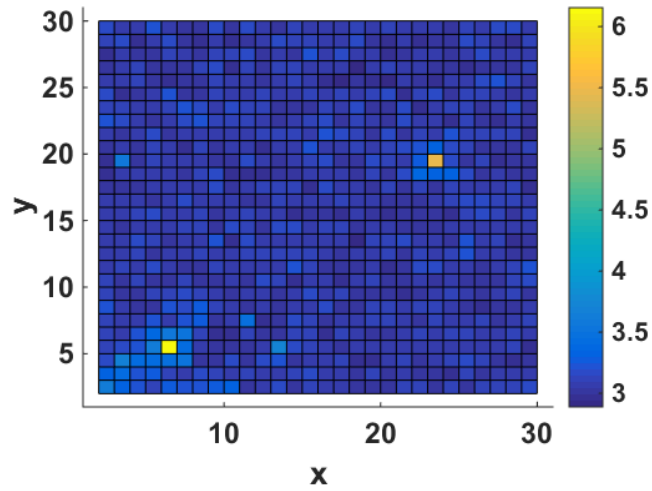


Figure 5.4 Spatial distributions of time kurtosis in Phase 2.

As seen in the above example, TR source localization with time kurtosis only needs one step: plot the spatial distributions of the time kurtosis computed in Phase 2. Thus, time kurtosis directly presents the results of the locations, while the space kurtosis method has to deal with and discard invalid local maxima. In other words, the reconstructed source locations (i_q, j_q) can be determined directly by [99]:

$$(i_q, j_q) = (i, j) | \beta_t(i, j) > B_t, q = 1, 2, \dots \quad (5.2a)$$

In the three-dimensional cases, this direct algorithm can be written as:

$$(i_q, j_q, k_q) = (i, j, k) | \beta_t(i, j, k) > B_t, q = 1, 2, \dots \quad (5.2b)$$

5.5 SUMMARY

The proposed kurtosis methods, which take the average field value into computation, are alternative methods for source reconstruction. Two types of kurtosis are introduced in this chapter: space kurtosis which works in a way similar to entropy, and time kurtosis which is more efficient. The temporal distributions of space kurtosis identify the source's excitation time instants, while the spatial distributions of time kurtosis reconstruct the locations of sources directly. As a result, they present a full source reconstruction in time and space, which has not been seen in literature so far.

Finally, it is noted that the kurtosis methods perform better than the entropy in general since they are more noise-resistant; the reason is that the field averaging is involved in the kurtosis computations, as shown in (5.1).

CHAPTER 6 EXPERIMENTAL VALIDATIONS

6.1 INTRODUCTION

Although the TR method has been attractive in electromagnetic and microwave research, previous studies mostly focus on numerical simulations in ideal conditions. In real testing and experiments, applying TR to radio frequency (RF) signals is more difficult than that in acoustics; factors like working bandwidth and upper frequency of sources and testing equipment need to be considered. As a result, little has been reported so far on electromagnetic hardware experimental validations of the TR method. In this chapter, we will present experimental validations of the TR method based on the previous chapters.

6.2 THE TESTING EQUIPMENT

In this section, we briefly describe the testing equipment and the components we used for the experimental validation.

The antenna is a device that interfaces electronics and electromagnetic fields in free space. It transmits or receives electromagnetic signals. There are many types of antennas. Commonly seen antennas include wire antenna, surface antenna, loop antenna, patch antenna, slot antenna, reflector antenna, array antenna, and so on. In our measurements, we use the wire antenna for its simple structure and easy fabrication.

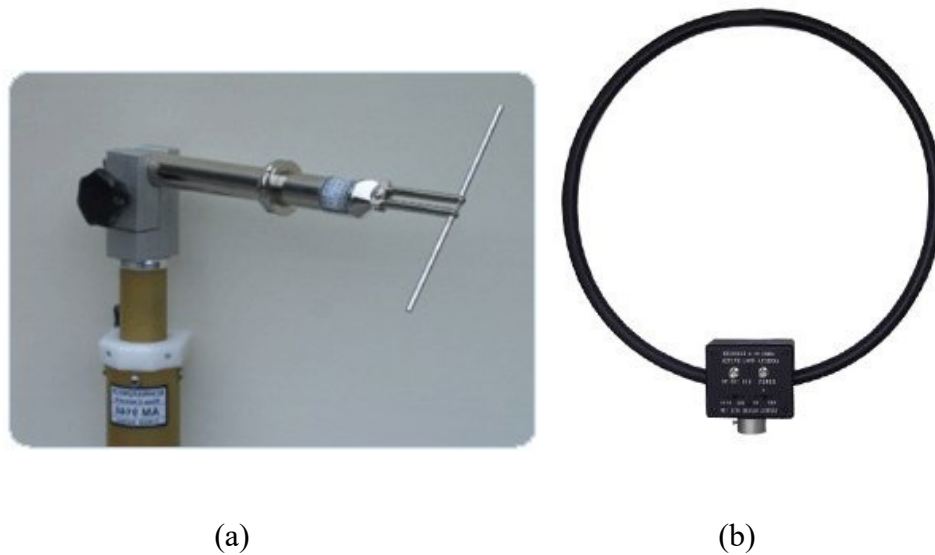


Figure 6.1 Typical antennas. (a) Dipole antenna. (b) Loop antenna.

The oscilloscope is an instrument that records and displays the waveform of a signal in the time domain. Bandwidth is its vital parameter; it is decided by the analog bandwidth of the amplifier used in the oscilloscope. If the bandwidth of a signal exceeds that of an oscilloscope, the signal with a larger rise time [89] will appear on the screen, and we will lose accuracy in testing.

The vector network analyzer (VNA) is a precise, active instrument working in the frequency domain. Its output is usually a wide-band RF source (e.g., Gaussian pulse). It sends a signal through one port to a network (or a propagation channel) and receives the signal that passes through the network by another port. With the signal sent at one port and received at another port, a scattering parameter matrix is automatically computed and shown on the screen. The scattering parameters describe the relationship between the incident and the reflected waves between the two ports. As the reference source (the output) is usually a low-power RF signal, VNA can be used for the accurate measurement of weak signals (compared with high voltage) within a higher frequency band (e.g., 10 to 50 GHz) than the oscilloscope. Thus, VNA is preferred over the oscilloscope in experiments and is

sufficient for the validations of temporal and spatial concentration when normalized field intensity is considered.

6.3 THE TR EXPERIMENTAL SETUP

For experimental validations of our proposed TR, we need first to set up a testing system capable of verifying the spatial and temporal focusing in source reconstruction. Dyab's team discusses the difficulties of directly applying TR to microwave signals in the time domain (e.g., using an oscilloscope). They propose a workaround to conduct measurements in the frequency domain using a VNA and applying the Hilbert transform to overcome the causality issues [10].

In the TR method, the operations are conducted in the time domain. In the cases we studied before, we employ wide-band time-domain signals recorded at TRM. In reality, we have band-limited frequency-domain signals due to the equipment's restricted frequency bands (e.g., a VNA). Therefore, we need to transform them into the proper time-domain signals, which can then be used in Phase 2 of the TR method. However, if we apply the inverse Fourier transform (IFT) directly to band-limited signals, we will obtain non-causal complex time-domain signals, which are not usable for the TR computation. Thus, we propose the following algorithms to address this problem.

6.3.1 The Algorithms for Handling Band-Limited Data

Suppose that we obtain the measured frequency domain result from the VNA is $S_{pq}[k_f]$; k_f is the discrete sampling frequency, which corresponds to the real frequency of $k_f/N\Delta t$. To emulate the band-limited testing data by the equipment here, we define the band-limited signal $S_{pq}^c[k_f]$ by cutting off $S_{pq}[k_f]$ outside $[k_L, k_H]$; that is, we have the following band-limited signal as follows:

$$S_{pq}^c[k_f] = \begin{cases} S_{pq}[k_f], & k_f \in [k_L, k_H] \\ 0, & k_f \notin [k_L, k_H] \end{cases} \quad (6.1)$$

$[k_L, k_H]$ is the working bandwidth of the equipment.

Based on the IFT of $S_{pq}^c[k_f]$, we propose the following algorithms to reconstruct the causal time-domain signals from the band-limited frequency-domain testing data:

$$y_p^c[n] = \sum_{k_f=k_L}^{k_H} |S_{pq}[k_f]| \cos\left(2\pi n \frac{k_f}{N} + \angle S_{pq}[k_f]\right), \quad (6.2a)$$

or

$$y_p^c[n] = \sum_{k_f=k_L}^{k_H} |S_{pq}[k_f]| \sin\left(2\pi n \frac{k_f}{N} + \angle S_{pq}[k_f]\right). \quad (6.2b)$$

N is the same as the total number of the time steps introduced in the TR simulation.

Signals (6.2a) and (6.2b) correspond to the real part and imaginary part of the IFT of $S_{pq}^c[k_f]$; their spectra in the frequency domain are the same as that of $S_{pq}^c[k_f]$. Either one of the signals of (6.2) can be time-reversed and then re-injected at TRM in Phase 2 for source reconstruction as computed by

$$y_p^r(t) = y_p^c\{(N-n)\Delta t\}. \quad (6.3)$$

6.3.2 The Testing Diagram

The testing diagram for experimental validations is shown in Figure 6.2.

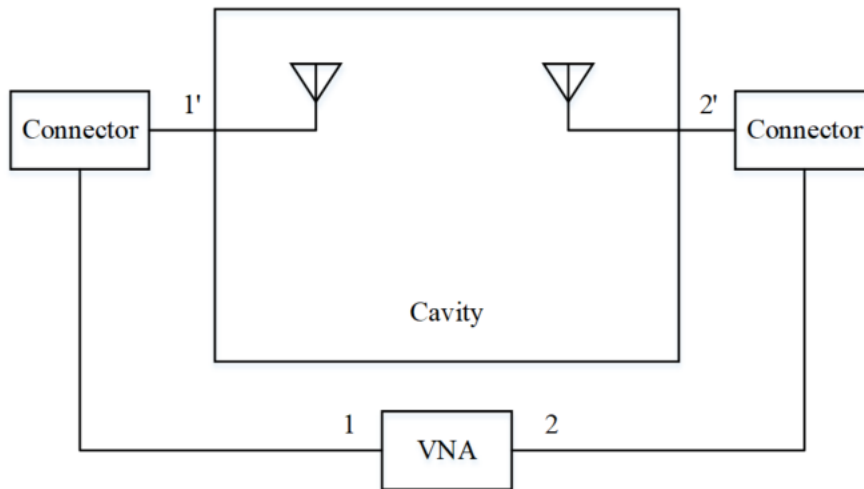


Figure 6.2 The diagram of the test setup.

A cavity is used as the test enclosure. Two probe antennas are placed inside the cavity. One antenna is connected to Port 1 of the VNA through connector 1', and another antenna to Port 2 through connector 2'. The antenna connected to Port 1 serves as the source, and the antenna connected to Port 2 serves the TRM sensor. The connectors are installed on the boundaries of the cavity. The VNA is connected to the connectors through coaxial cables. Note that we can move the positions of the antennas; this would correspond to positioning the source and TRM sensors at different locations.

In measurements, the VNA generates a band-limited electromagnetic signal out from Port 1. The signal transmits through the cable, connector 1' to the antenna on the left inside the cavity. Then the electromagnetic field is excited and propagates inside the cavity, and the antenna on the right receives it. The signal received is then sent to Port 2 of the VNA through the cable and measured. The scattering parameters (S_{21}), which correspond to the frequency-domain transfer function between the two antennas in the cavity, are computed and displayed on the VNA. We can then use the proposed algorithms of (6.2) to transform the band-limited scattering parameters into usable time-domain signals, which are the impulse responses between the two antennas.

6.3.3 Reciprocity

Reciprocity is an essential requirement for the TR process. Since our test is conducted in an air-filled cavity bounded by PEC walls, the reciprocity theorem in electromagnetics [88, 111] can ensure the reciprocity of the signals between the ports or between the source and TRM antennas. More specifically, if the source at point A generates a field at point B, the same field at point A will be generated by the same source at point B. As a result, in the TR computations of Phase 2, if we inject the time-reversed signal of (6.3) into the cavity through Port 2', we expect to get a field concentration at Port 1' (the source location).

6.4 THE CONFORMAL FDTD MODELING

The conventional FDTD scheme uses cubic meshes. Such numerical meshes are not conformal to the cross-sections of monopole probe antennas which can be circular, causing so-called staircase errors. Thus, modifications of the FDTD meshes are required to ensure the accuracy of modelling and computation. The relevant techniques have been proposed with the finite-integration method. Two of them, the contour path (CP) and the sub-gridding methods, are briefly described in the following subsections.

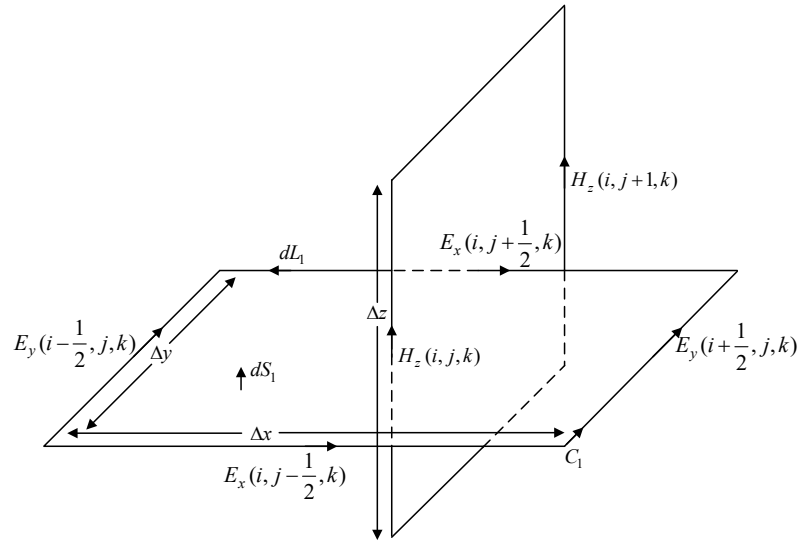
6.4.1 The Contour Path (CP) Method

The CP method is based on the integral Maxwell's equations, which was first proposed by Taflove and his collaborators [112]. The main advantage of the CP method is its arbitrary contour-based mesh. Therefore, it is widely applied to simulating curved surfaces in the Cartesian coordinate system.

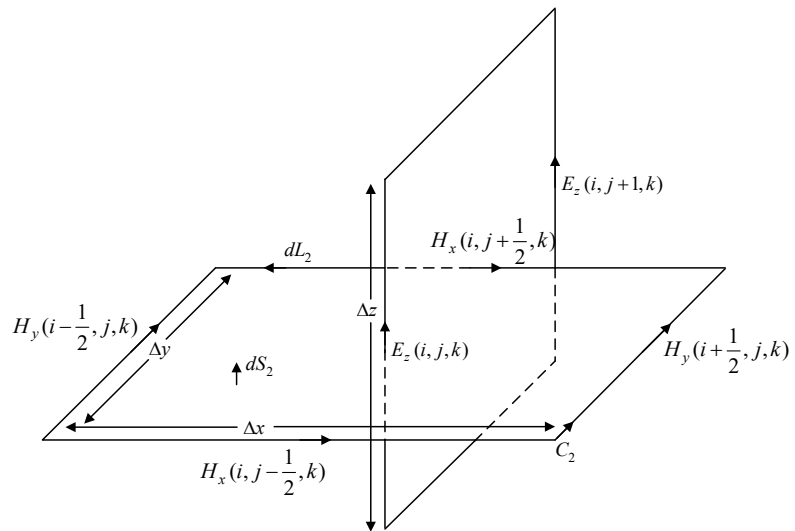
Consider the integral Maxwell's equations of Yee's electric or magnetic loop in Figure 6.3:

$$\frac{\partial}{\partial t} \int_S \mathbf{H} \cdot d\mathbf{s} = -\frac{1}{\mu} \oint_C \mathbf{E} \cdot d\mathbf{l}, \quad (6.4a)$$

$$\frac{\partial}{\partial t} \int_S \mathbf{E} \cdot d\mathbf{s} = + \frac{1}{\epsilon} \oint_C \mathbf{H} \cdot d\mathbf{l}. \quad (6.4b)$$



(a)



(b)

Figure 6.3 Typical Yee's lattices. (a) Electric loop. (b) Magnetic loop.

Take Faraday's law of (6.4a) as an example. We apply it to the contour path C_1 shown in

Figure 6.3(a). We choose $H_z(i, j, k)$ as the averaged magnetic field on plane S_1 and electric fields at the center point of each side of C_1 as the corresponding averaged electric field components. After replacing the time derivative with its central finite difference approximation, we have

$$\frac{H_z(i, j, k, n+1/2) - H_z(i, j, k, n-1/2)}{\Delta t} \Delta x \Delta y = -\frac{1}{\mu} \left[E_x(i, j - \frac{1}{2}, k, n) \Delta x + E_y(i + \frac{1}{2}, j, k, n) \Delta y - E_x(i, j + \frac{1}{2}, k, n) \Delta x - E_y(i - \frac{1}{2}, j, k, n) \Delta y \right]. \quad (6.5)$$

This equals to (2.4c) when $\Delta x = \Delta y = \delta$, which means that the same FDTD scheme can be derived either from differential or integral Maxwell's equations.

Since the CP method can be applied to an arbitrary loop, we will have a more general form of (6.6):

$$H_z(i, j, k, n + \frac{1}{2}) = H_z(i, j, k, n - \frac{1}{2}) - \frac{\Delta t}{S\mu(i, j, k)} \left[E_x(i, j - \frac{1}{2}, k, n) l_1 + E_y(i + \frac{1}{2}, j, k, n) l_2 - E_x(i, j + \frac{1}{2}, k, n) l_3 - E_y(i - \frac{1}{2}, j, k, n) l_4 \right]. \quad (6.6)$$

Here, S is the area of S_1 , l_1 , l_2 , l_3 and l_4 are the lengths of each side of the contour.

Other field components can also be derived similarly by employing the integral form of Maxwell's equations. The resulting finite-difference equations can then be applied to curved surfaces of cylindrical antennas.

6.4.2 The Sub-Gridding Technique

The CP method enables us to simulate cylindrical antennas in the Cartesian coordinate system. However, the radius of a wire antenna is usually much smaller than the cell size of Yee's lattice. In such a case, the CP method is not effective and efficient. Taflove introduced different algorithms to deal with such problems [112]. The algorithms are summarized as

the sub-gridding technique.

Take the thin wire conductor shown in Figure 6.4.

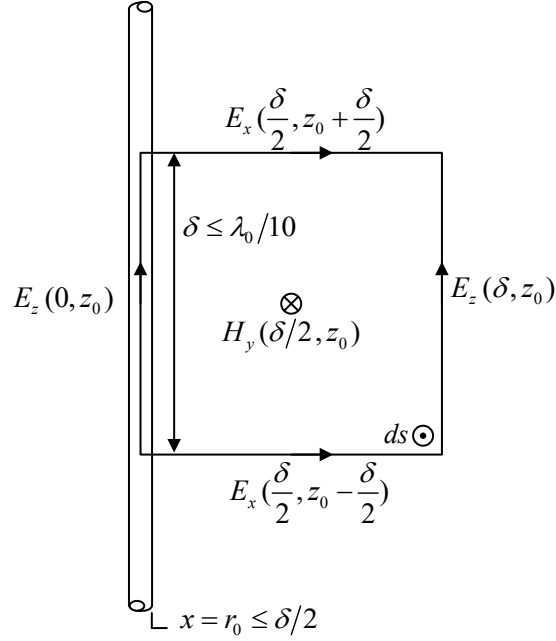


Figure 6.4 The thin wire model.

The components of circumferential magnetic field and radial electric field vary as $1/r$ near the wire, where r is the distance from the wire center and r_0 is the radius of the wire; after applying Faraday's law to the contour path as shown in Figure 6.4, we can get [112]:

$$\frac{H_y(\delta/2, z_0, n+1/2) - H_y(\delta/2, z_0, n-1/2)}{\Delta t} \approx \left\{ \left[E_x\left(\frac{\delta}{2}, z_0 - \frac{\delta}{2}, n\right) - E_x\left(\frac{\delta}{2}, z_0 + \frac{\delta}{2}, n\right) \right] \cdot \frac{1}{2} \ln\left(\frac{\delta}{r_0}\right) + E_z(\delta, z_0, n) \right\} / \left\{ \mu_0 \frac{\delta}{2} \ln\left(\frac{\delta}{r_0}\right) \right\}. \quad (6.7)$$

Computation of other field components and other applications can be derived similarly, and readers are referred to Taflove's work [112] for more details.

With the CP method and the sub-gridding technique developed above, we can handle the

modelling of wire probe antennas for the TR computations.

The above conformal FDTD modelling techniques are implemented in the commercially available software package called CST Microwave Studio. We use the package for our experimental validations of the TR method.

6.5 THE EXPERIMENTAL VALIDATION RESULTS

6.5.1 Experimental Hardware Setup

As aforementioned, we fabricate a cavity for verification. The cavity is a box of 250mm×150mm×100mm in dimensions. It has seven holes for installing the probes at different locations (to emulate the sources and the TRM). If any holes are used, they will be mounted with a monopole antenna with a connector; any other holes are sealed off with a metal patch if they are not used. Any pair of the used holes are electrically considered as the ports of 1' or 2' as indicated in Figure 6.2. The photo of the prototype is shown in Figure 6.6.

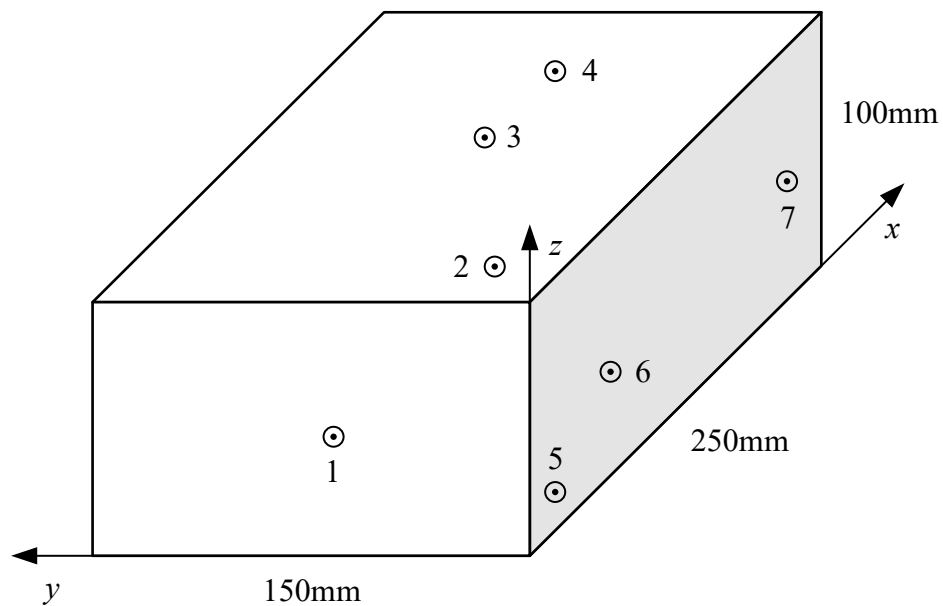


Figure 6.5 The physical dimensions of the cavity developed.



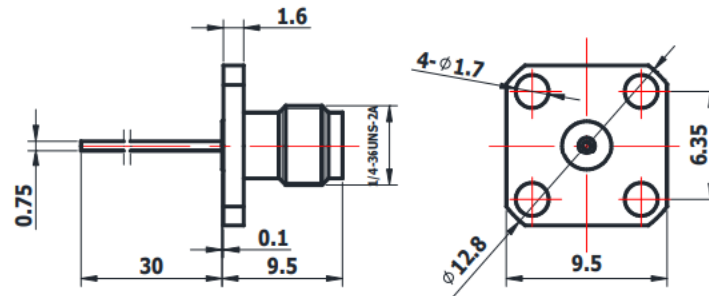
Figure 6.6 The photo of the cavity.

We also number each hole (or port) for measurements. Positions of each port is shown in Table 6.1 below:

Table 6.1 Positions of each port.

Port	x/mm	y/mm	z/mm
1	0	70	50
2	30	30	100
3	130	74	100
4	200	74	100
5	20	0	20
6	80	0	50
7	210	0	50

The commercial software package, CST Microwave Studio, is used to model this cavity with monopole antennas 30 mm in length. The coaxial probe integrated with the connector shown in Figure 6.7 is employed as the source and the TRM sensor. Its dimensions are also presented in Figure 6.7.



*Dimensions are in mm

(a)



(b)

Figure 6.7 2.92mm female connector with the probe antenna. (a) Structure and parameters. (b) Photo of the probe antenna.

6.5.2 Experimental Results

We first consider Port 3 as the input and Port 2 as the output. The experimental setup is shown in Figure 6.8. S_{23} is then obtained by the VNA; it is in the frequency domain and transformed to the time-domain response using the techniques described in Section 6.3.1.

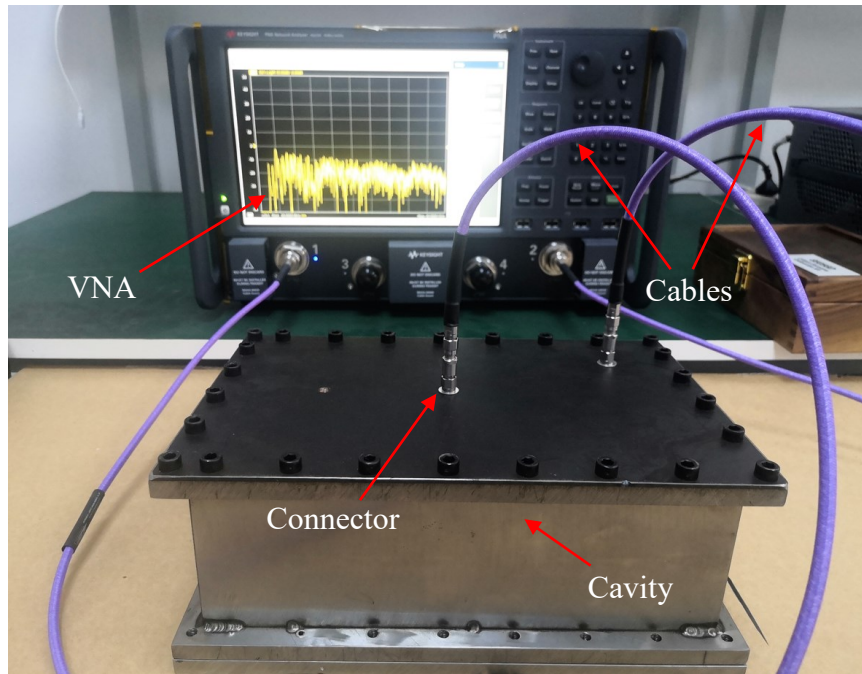


Figure 6.8 Photo of the hardware setup and measurement.



Figure 6.9 Screenshot of the CST simulation model.

Once the time-domain response of (6.2) is obtained, it is time-reversed by (6.3) and can be seen in Figure 6.10.

We use this signal as the excitation of Port 2 in our CST model and conduct the TR

simulation. The electric field distributions are shown in Figure 6.11.

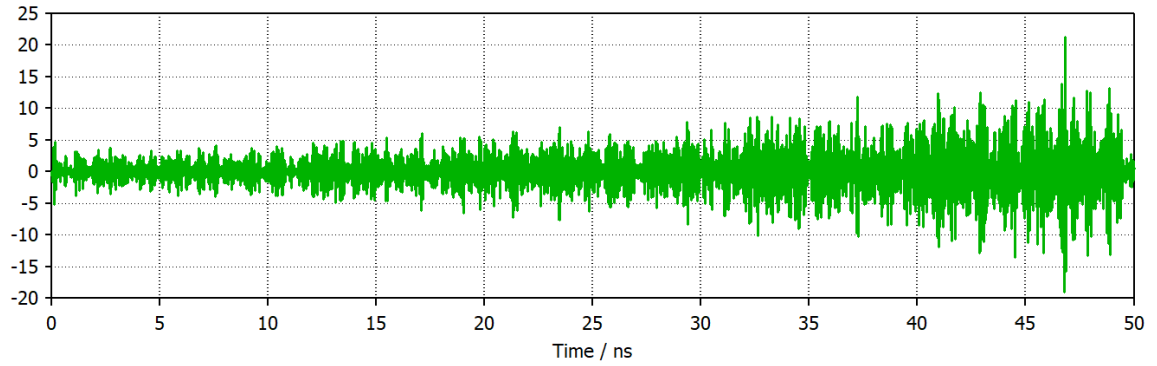
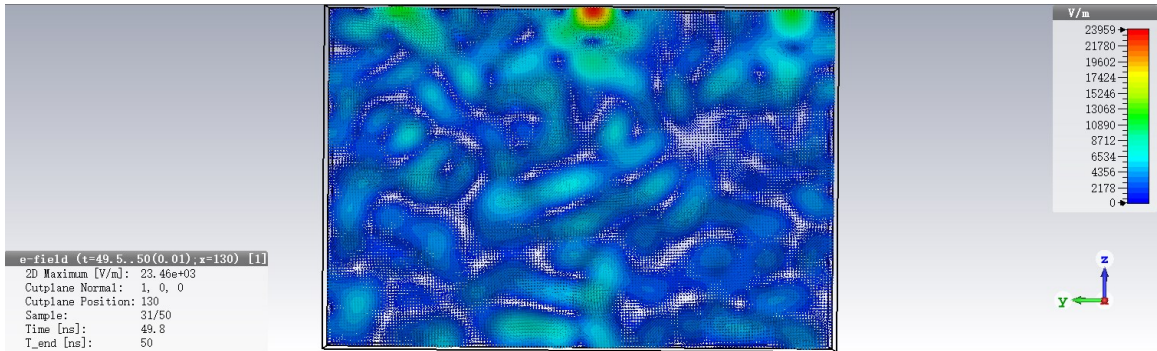
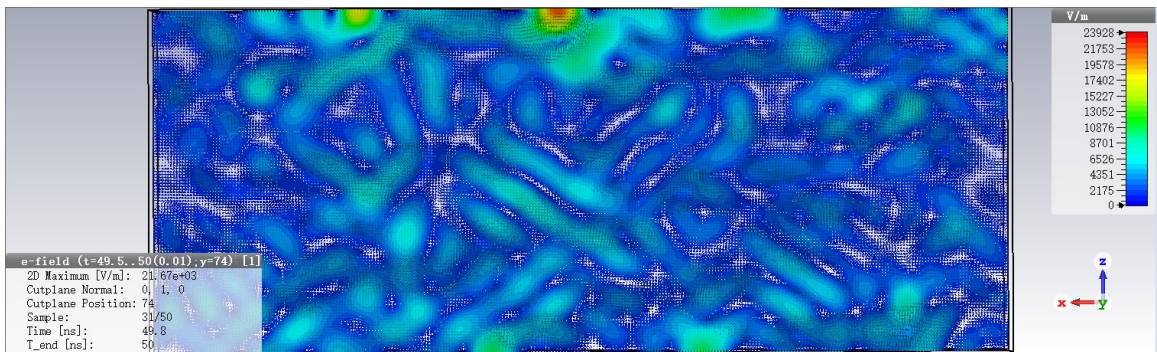


Figure 6.10 The time-reversed signal that is injected into the cavity.



(a)



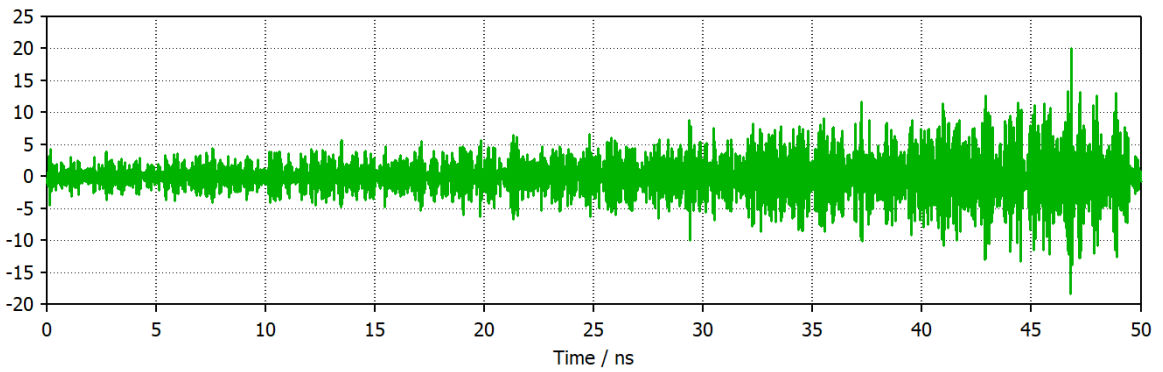
(b)

Figure 6.11 Electric field distributions with field concentration. (a) $x = 130$ mm plane. (b) $y = 74$ mm plane.

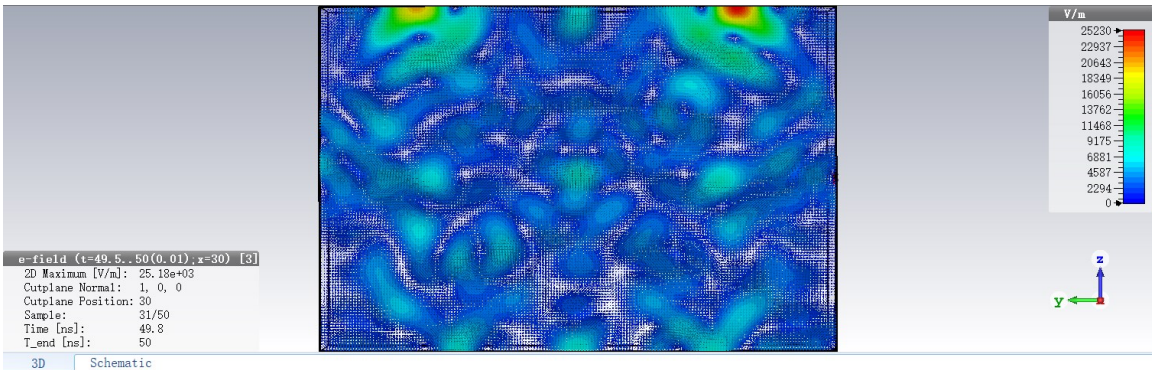
The highlighted region with deep red color in Figure 6.11 indicates the field concentration which corresponds to the location of Port 3 (representing the source location); this validates our TR with measurements successfully.

6.5.3 Validations with Two Sensors

In this part, we consider Port 2 as the input, Port 3 and Port 6 as the outputs. If we only use S_{32} for the TR computation, the results can be seen in Figure 6.12.



(a)



(b)

Figure 6.12 The TR results with only one TRM (Port 3). (a) Time-reversed signal. (b) TR source reconstruction results.

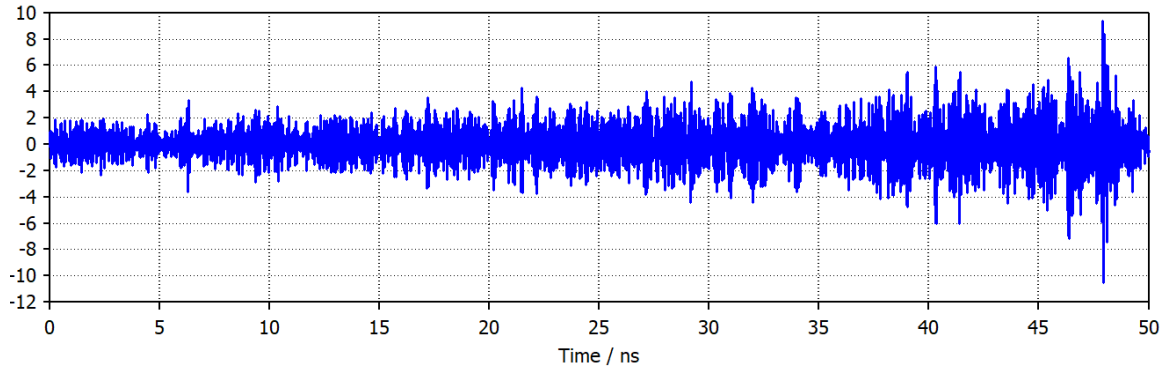
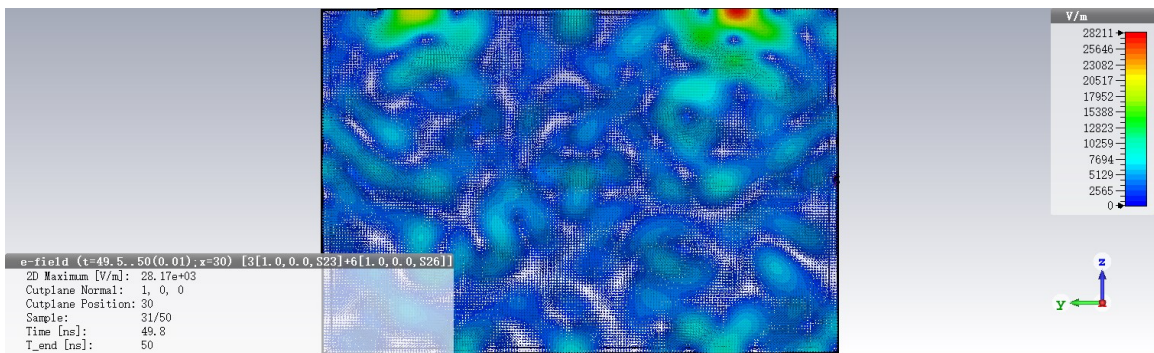
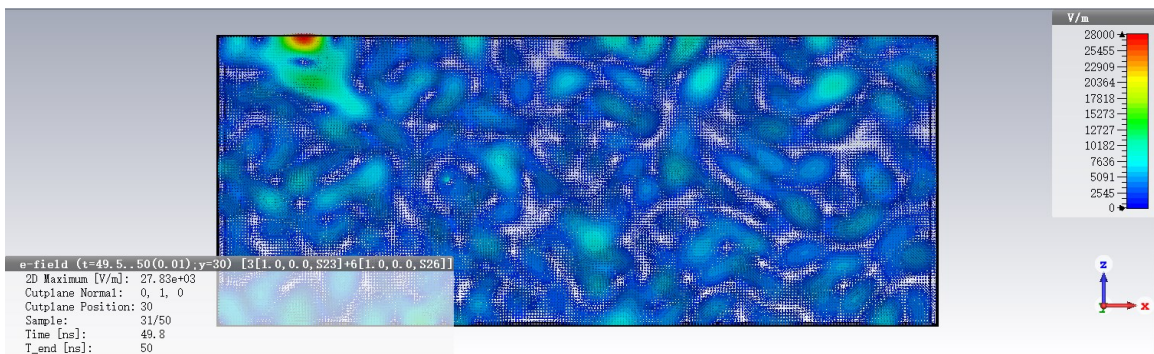


Figure 6.13 Time-reversed signal obtained from S_{62} .



(a)



(b)

Figure 6.14 The TR field distribution results with two sensors. (a) $x = 30\text{mm}$ plane. (b) $y = 30\text{mm}$ plane.

With the data obtained from Port 6 (S_{62}), we can get another time-reversed signal shown in

Figure 6.13, and the source reconstruction results with two TRM sensors are shown in Figure 6.14. By comparing Figure 6.12(b) and Figure 6.14(a), we can see that more prominent field concentration at Port 2 in Figure 6.14(a). This is the indication of better TR accuracy with two TRM sensors.

6.5.4 Discussions

We have validated the TR method with our experimental setup and measurements so far. There are still some phenomena and issues worth noting about the TR method. One of them is the bandwidth and related spatial resolution.

In the previous measurements, 10-20 GHz testing data is used for TR source reconstruction. Now we consider using a narrower frequency band of 5-10 GHz and conducting the same validation process. Results are shown in Figure 6.15 and 6.16:

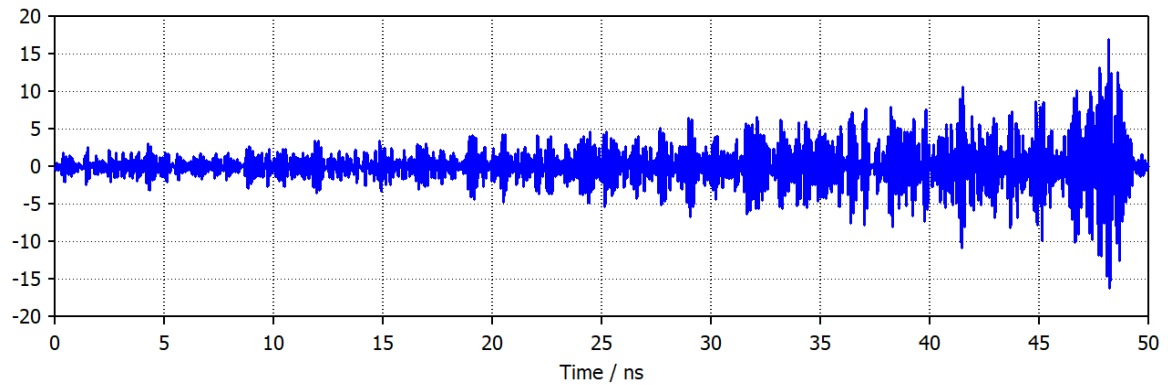
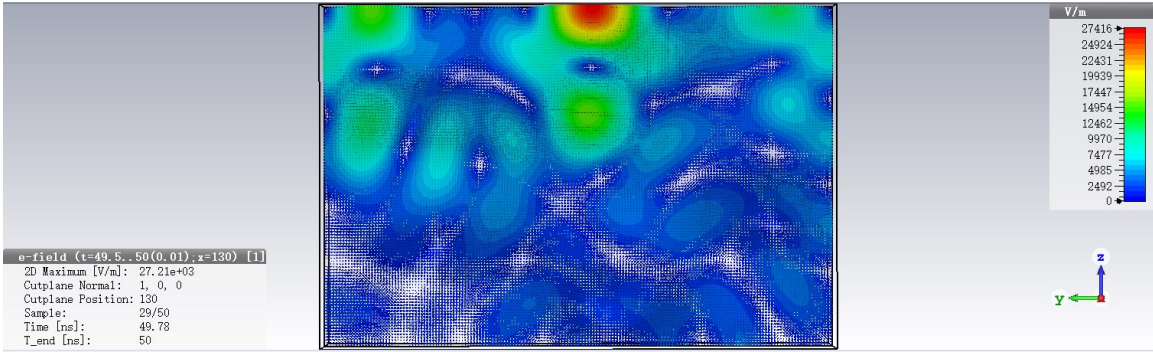
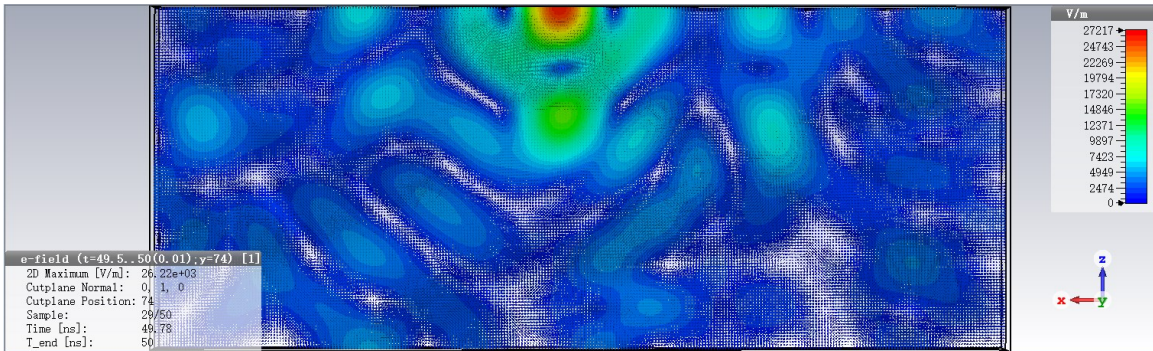


Figure 6.15 The time-reversed signal (5-10 GHz) that is injected into the CST model.



(a)



(b)

Figure 6.16 Electric field distributions when the concentration occurs. (a) $x = 130\text{mm}$ plane. (b) $y = 74\text{mm}$ plane.

The injected signal Figure 6.15 is similar to that in Figure 6.10, but without information of frequencies higher than 10 GHz. Figure 6.16 shows that the recovered source red region is about twice wider as that of Figure 6.11; this meets the theoretical expectation of higher frequency and better spatial resolution [86]. In other words, Rayleigh resolution ($\lambda_{\min}/2$) is the highest accuracy that we can recover based on our testing bandwidth and upper frequency.

6.6 SUMMARY

Previous TR research mainly focused on numerical simulations or other applications in areas like acoustics. Little has been done in experimental verifications of the TR method. In this chapter, we start with an experimental hardware design to validate our TR method discussed in Chapters 2 and 3. We propose the use of a VNA and a cavity to conduct the validation. We develop the algorithms to convert a frequency-domain measurement signal to a time-domain signal that is useful for the TR computation. By employing the CST Microwave Studio, we can carry out the TR source reconstruction with the measurement data. Thus we verify the effectiveness of the TR method experimentally.

The observation of the spatial focus is demonstrated for the first time. It shows that Rayleigh resolution ($\lambda_{\min}/2$) is the highest accuracy that we can recover a source by TR. Two overlapped sources may result in errors in reconstruction; this leads to future work on the validations of multiple sources reconstruction where further experiments and simulations are needed. Furthermore, potential algorithms and methods for distinguishing closely located sources will lead to another topic on the fundamentals and applications of super-resolution [31, 46, 51, 63].

In summary, the work presented in this chapter lays the groundwork for future practical applications of the TR method to realistic problems such as EMI source identification.

CHAPTER 7 CONCLUSION

7.1 CONCLUDING REMARKS

In this thesis, we investigate a broad range of TR topics that include theories, algorithms, simulations, and experimentations. We first discuss the fundamentals of TR in electromagnetics and then introduce a cavity for the TR computation in our case. We provide a new explanation of the TR source reconstruction and present the following advantages of the TR in a cavity: first, it is applicable to real problems compared to other passive TR methods; secondly, one TRM element is sufficient to recover the sources with good resolution; thirdly, only one type of the TRM probe (electric or magnetic) is needed, which saves the computational or experimental resources; fourthly, the cavity preserves the energy and contains rich multipath field components that are much desired with the TR method.

Unlike the conventional TR method, the TR method proposed in this thesis can recover multiple sources. Inspired by the ideas in statistical data analysis, we then develop entropy and kurtosis methods for the TR source reconstruction. They allow the identification of multiple transient sources excited at unknown time instants. The effectiveness of these methods is verified with numerical experiments conducted with the FDTD method. We also propose the threshold criterion to avoid false solutions for a faster and more efficient TR process.

Finally, we design and conduct a hardware experiment to validate the TR method, which has not been seen in the literature so far. The CST Microwave Studio is used to process the measurement data and recover the sources. Results verify the effectiveness of the TR method experimentally, laying the groundwork for the applications of the TR method to realistic problems.

It is worth mentioning that the work of this thesis has been published in [99, 104, 105].

7.2 FUTURE WORK

Although the work presented in this thesis is quite broad, it is more or less preliminary. Future in-depth research may follow the following directions.

The first is the study of bandwidth and spatial resolution for the TR. In our numerical examples, wide-band excitations (e.g., impulse source) result in a perfect concentration and source reconstruction in ideal conditions; They also contribute to good performances of entropy and kurtosis methods. However, in the real world, only band-limited information is available; it restricts the spatial resolution of the TR source reconstruction and affects the performances of entropy and kurtosis. In addition, since we use a cavity to conduct the TR source reconstruction, how to take advantage of the ergodic properties to speed up the TR computation is a topic of interest. Further research along all these lines is needed.

Secondly, our experimental design aims at basic validations of TR, so we choose monopole antennas for simplicity. Other antennas or probes have different properties like working bandwidth, directivity, and polarization. Experimentations with different antennas may have different performances and phenomena. Also, there have been studies on the reconstruction of clustered sources and diagnosis of faulty antenna elements [84]; TR applications along this line are also an interesting topic.

Thirdly, we do not consider noise in this thesis because our TR is conducted in a cavity. The TR in a partially open cavity may suffer from performance degradations by noise [113]. Therefore, theoretical studies on the effects of noise and related noise-mitigation techniques are much desired.

Fourthly, structure synthesis of scatterers with the TR method is another interesting and

important topic. The success of the TR structure synthesis can lead to a potential revolution in electromagnetic designs, including RF/microwave circuit designs and applications.

Finally, more extensive testing and experiments (e.g., reconstruction of multiple asynchronous sources, arbitrarily shaped sources, and source reconstruction in the frequency domain) are still needed to have more understanding and applications of the TR method for real-world applications. They are still appealing for future research.

BIBLIOGRAPHY

- [1] Taflove, A., & Hagness, S. C. (2005). *Computational electrodynamics: the finite-difference time-domain method*. Artech house.
- [2] Yee, K. (1966). Numerical solution of initial boundary value problems involving Maxwell's equations in isotropic media. *IEEE Transactions on antennas and propagation*, 14(3), 302-307.
- [3] Taflove, A., & Brodwin, M. E. (1975). Numerical solution of steady-state electromagnetic scattering problems using the time-dependent Maxwell's equations. *IEEE transactions on microwave theory and techniques*, 23(8), 623-630.
- [4] Taflove, A., & Brodwin, M. E. (1975). Computation of the electromagnetic fields and induced temperatures within a model of the microwave-irradiated human eye. *IEEE Transactions on Microwave Theory and Techniques*, 23(11), 888-896.
- [5] Taflove, A. (1980). Application of the finite-difference time-domain method to sinusoidal steady-state electromagnetic-penetration problems. *IEEE Transactions on electromagnetic compatibility*, (3), 191-202.
- [6] Taflove, A. (1988). Review of the formulation and applications of the finite-difference time-domain method for numerical modeling of electromagnetic wave interactions with arbitrary structures. *Wave Motion*, 10(6), 547-582.
- [7] Gedney, S. D. (2011). Introduction to the finite-difference time-domain (FDTD) method for electromagnetics. *Synthesis Lectures on Computational Electromagnetics*, 6(1), 1-250.
- [8] Sorrentino, R., Roselli, L., & Mezzanotte, P. (1993). Time reversal in finite difference time domain method. *IEEE Microwave and Guided wave letters*, 3(11), 402-404.
- [9] Cepni, A. (2005). *Experimental investigation of time-reversal techniques using electromagnetic waves* (Doctoral dissertation, Ph. D. dissertation, Dep. Elect. Comp. Eng., Carnegie Mellon Univ., Pittsburgh, PA).
- [10] Dyab, W. M. G., Sarkar, T. K., García-Lampérez, A., Salazar-Palma, M., & Lagunas, M. A. (2013). A critical look at the principles of electromagnetic time reversal and its consequences. *IEEE Antennas and Propagation Magazine*, 55(5), 28-62.

- [11] Bogert, B. (1957). Demonstration of delay distortion correction by time-reversal techniques. *IRE Transactions on Communications Systems*, 5(3), 2-7.
- [12] Fink, M. (1992). Time reversal of ultrasonic fields. I. Basic principles. *IEEE transactions on ultrasonics, ferroelectrics, and frequency control*, 39(5), 555-566.
- [13] Wu, F., Thomas, J. L., & Fink, M. (1992). Time reversal of ultrasonic fields. II. Experimental results. *IEEE transactions on ultrasonics, ferroelectrics, and frequency control*, 39(5), 567-578.
- [14] Cassereau, D., & Fink, M. (1992). Time-reversal of ultrasonic fields. III. Theory of the closed time-reversal cavity. *IEEE transactions on ultrasonics, ferroelectrics, and frequency control*, 39(5), 579-592.
- [15] Oestges, C., Kim, A. D., Papanicolaou, G., & Paulraj, A. J. (2005). Characterization of space-time focusing in time-reversed random fields. *IEEE transactions on antennas and propagation*, 53(1), 283-293.
- [16] Kosmas, P., & Rappaport, C. M. (2005). Time reversal with the FDTD method for microwave breast cancer detection. *IEEE Transactions on Microwave Theory and Techniques*, 53(7), 2317-2323.
- [17] Kosmas, P., & Rappaport, C. M. (2006). FDTD-based time reversal for microwave breast cancer detection-localization in three dimensions. *IEEE Transactions on Microwave Theory and Techniques*, 54(4), 1921-1927.
- [18] Kosmas, P., & Rappaport, C. M. (2006). A matched-filter FDTD-based time reversal approach for microwave breast cancer detection. *IEEE Transactions on Antennas and Propagation*, 54(4), 1257-1264.
- [19] Fan, W. (2017). *Development and Application of the Finite Difference Time Domain (FDTD) Method* (Ph.D. dissertation, Dept. Elect. & Comp. Eng., Dalhousie Univ., Halifax, NS, Canada).
- [20] Parsons, J. D. (2000). *The mobile radio propagation channel*. Wiley.
- [21] Foschini, G. J., & Gans, M. J. (1998). On limits of wireless communications in a fading environment when using multiple antennas. *Wireless personal communications*, 6(3), 311-335.

- [22] Shiu, D. S., Foschini, G. J., Gans, M. J., & Kahn, J. M. (2000). Fading correlation and its effect on the capacity of multielement antenna systems. *IEEE Transactions on communications*, 48(3), 502-513.
- [23] Paulraj, A. J., Gore, D. A., Nabar, R. U., & Bolcskei, H. (2004). An overview of MIMO communications—a key to gigabit wireless. *Proceedings of the IEEE*, 92(2), 198-218.
- [24] Paulraj, A. J., & Ng, B. C. (1998). Space-time modems for wireless personal communications. *IEEE Personal Communications*, 5(1), 36-48.
- [25] Poon, A. S., Brodersen, R. W., & Tse, D. N. (2005). Degrees of freedom in multiple-antenna channels: A signal space approach. *IEEE Transactions on Information Theory*, 51(2), 523-536.
- [26] Wallace, J. W., Jensen, M. A., Swindlehurst, A. L., & Jeffs, B. D. (2003). Experimental characterization of the MIMO wireless channel: Data acquisition and analysis. *IEEE Transactions on Wireless Communications*, 2(2), 335-343.
- [27] Cepni, A. G., Stancil, D. D., Xhafa, A. E., Henty, B., Nikitin, P. V., Tonguz, O. K., & Brodtkorb, D. (2004, June). Capacity of multi-antenna array systems for HVAC ducts. In *2004 IEEE International Conference on Communications (IEEE Cat. No. 04CH37577)* (Vol. 5, pp. 2934-2938). IEEE.
- [28] Born, M., & Wolf, E. (1970). Principles of optics, 1999. *Press Syndicated, Cambridge: UK*.
- [29] Pepper, D. M. (1985). Nonlinear optical phase conjugation. *Laser handbook*, 333-485.
- [30] Henty, B. E., & Stancil, D. D. (2004, June). Bandwidth limitations of phase-conjugate arrays used for multipath focusing. In *IEEE Antennas and Propagation Society Symposium, 2004*. (Vol. 3, pp. 2792-2795). IEEE.
- [31] Henty, B. E., & Stancil, D. D. (2004). Multipath-enabled super-resolution for rf and microwave communication using phase-conjugate arrays. *Physical Review Letters*, 93(24), 243904.
- [32] Fink, M., Prada, C., Wu, F., & Cassereau, D. (1989, October). Self focusing in inhomogeneous media with time reversal acoustic mirrors. In *Proceedings., IEEE Ultrasonics Symposium*, (pp. 681-686). IEEE.

- [33] Prada, C., Wu, F., & Fink, M. (1991). The iterative time reversal mirror: A solution to self-focusing in the pulse echo mode. *The Journal of the Acoustical Society of America*, 90(2), 1119-1129.
- [34] Fink, M. (1993). Time-reversal mirrors. *Journal of Physics D: Applied Physics*, 26(9), 1333.
- [35] Prada, C., Thomas, J. L., & Fink, M. (1995). The iterative time reversal process: Analysis of the convergence. *The Journal of the Acoustical Society of America*, 97(1), 62-71.
- [36] Derode, A., Roux, P., & Fink, M. (1995). Robust acoustic time reversal with high-order multiple scattering. *Physical review letters*, 75(23), 4206.
- [37] Prada, C., Manneville, S., Spoliansky, D., & Fink, M. (1996). Decomposition of the time reversal operator: Detection and selective focusing on two scatterers. *The Journal of the Acoustical Society of America*, 99(4), 2067-2076.
- [38] Kerbrat, E., Prada, C., Cassereau, D., & Fink, M. (2002). Ultrasonic nondestructive testing of scattering media using the decomposition of the time-reversal operator. *IEEE Transactions on ultrasonics, ferroelectrics, and frequency control*, 49(8), 1103-1113.
- [39] Kuperman, W. A., & Lynch, J. F. (2004). Shallow-water acoustics. *Physics Today*, 57(10), 55-61.
- [40] Kim, S., Kuperman, W. A., Hodgkiss, W. S., Song, H. C., Edelmann, G. F., & Akal, T. (2003). Robust time reversal focusing in the ocean. *The Journal of the Acoustical Society of America*, 114(1), 145-157.
- [41] Edelmann, G. F., Akal, T., Hodgkiss, W. S., Kim, S., Kuperman, W. A., & Song, H. C. (2002). An initial demonstration of underwater acoustic communication using time reversal. *IEEE journal of oceanic engineering*, 27(3), 602-609.
- [42] Kuperman, W. A., Hodgkiss, W. S., Song, H. C., Akal, T., Ferla, C., & Jackson, D. R. (1998). Phase conjugation in the ocean: Experimental demonstration of an acoustic time-reversal mirror. *The journal of the Acoustical Society of America*, 103(1), 25-40.
- [43] Hodgkiss, W. S., Song, H. C., Kuperman, W. A., Akal, T., Ferla, C., & Jackson, D. R. (1999). A long-range and variable focus phase-conjugation experiment in shallow water. *The Journal of the Acoustical Society of America*, 105(3), 1597-1604.

- [44] Jackson, D. R., & Dowling, D. R. (1991). Phase conjugation in underwater acoustics. *The Journal of the Acoustical Society of America*, 89(1), 171-181.
- [45] Fink, M., Cassereau, D., Derode, A., Prada, C., Roux, P., Tanter, M., ... & Wu, F. (2000). Time-reversed acoustics. *Reports on progress in Physics*, 63(12), 1933.
- [46] Blomgren, P., Papanicolaou, G., & Zhao, H. (2002). Super-resolution in time-reversal acoustics. *The Journal of the Acoustical Society of America*, 111(1), 230-248.
- [47] Clouet, J. F., & Fouque, J. P. (1997). A time-reversal method for an acoustical pulse propagating in randomly layered media. *Wave Motion*, 25(4), 361-368.
- [48] Dowling, D. R., & Jackson, D. R. (1992). Narrow-band performance of phase-conjugate arrays in dynamic random media. *The Journal of the Acoustical Society of America*, 91(6), 3257-3277.
- [49] Asch, M., Kohler, W., Papanicolaou, G., Postel, M., & White, B. (1991). Frequency content of randomly scattered signals. *SIAM review*, 33(4), 519-625.
- [50] Kohler, W., Papanicolaou, G., & White, B. (1996). Localization and mode conversion for elastic waves in randomly layered media II. *Wave Motion*, 23(2), 181-201.
- [51] Tsogka, C., & Papanicolaou, G. C. (2002). Time reversal through a solid-liquid interface and super-resolution. *Inverse problems*, 18(6), 1639.
- [52] Papanicolaou, G., Solna, K., & Ryzhik, L. (2004). Statistical stability in time reversal. *SIAM Journal on Applied Mathematics*, 64(4), 1133-1155.
- [53] Borcea, L., Papanicolaou, G., Tsogka, C., & Berryman, J. (2002). Imaging and time reversal in random media. *Inverse Problems*, 18(5), 1247.
- [54] Prada, C., & Thomas, J. L. (2003). Experimental subwavelength localization of scatterers by decomposition of the time reversal operator interpreted as a covariance matrix. *The Journal of the Acoustical Society of America*, 114(1), 235-243.
- [55] Minonzio, J. G., Prada, C., Chambers, D., Clorennec, D., & Fink, M. (2005). Characterization of subwavelength elastic cylinders with the decomposition of the time-reversal operator: Theory and experiment. *The Journal of the Acoustical Society of America*, 117(2), 789-798.

- [56] Montaldo, G., Tanter, M., & Fink, M. (2002). Real time inverse filter focusing by iterative time reversal. *The Journal of the Acoustical Society of America*, 112(5), 2446-2446.
- [57] Montaldo, G., Tanter, M., & Fink, M. (2004). Revisiting iterative time reversal processing: Application to detection of multiple targets. *The Journal of the Acoustical Society of America*, 115(2), 776-784.
- [58] Prada, C., & Fink, M. (1994). Eigenmodes of the time reversal operator: A solution to selective focusing in multiple-target media. *Wave motion*, 20(2), 151-163.
- [59] Mordant, N., Prada, C., & Fink, M. (1999). Highly resolved detection and selective focusing in a waveguide using the DORT method. *The Journal of the Acoustical Society of America*, 105(5), 2634-2642.
- [60] Snieder, R. K., & Scales, J. A. (1998). Time-reversed imaging as a diagnostic of wave and particle chaos. *Physical Review E*, 58(5), 5668.
- [61] Hou, S., Solna, K., & Zhao, H. (2004). Imaging of location and geometry for extended targets using the response matrix. *Journal of Computational Physics*, 199(1), 317-338.
- [62] Lev-Ari, H., & Devaney, A. J. (2000, March). The time-reversal technique re-interpreted: Subspace-based signal processing for multi-static target location. In *Proceedings of the 2000 IEEE Sensor Array and Multichannel Signal Processing Workshop. SAM 2000 (Cat. No. 00EX410)* (pp. 509-513). IEEE.
- [63] Lehman, S. K., & Devaney, A. J. (2003). Transmission mode time-reversal super-resolution imaging. *The Journal of the Acoustical Society of America*, 113(5), 2742-2753.
- [64] Devaney, A. J., & Dennison, M. (2003). Inverse scattering in inhomogeneous background media. *Inverse Problems*, 19(4), 855.
- [65] Devaney, A. J., Marengo, E. A., & Gruber, F. K. (2005). Time-reversal-based imaging and inverse scattering of multiply scattering point targets. *The Journal of the Acoustical Society of America*, 118(5), 3129-3138.
- [66] Lerosey, G., De Rosny, J., Tourin, A., Derode, A., Montaldo, G., & Fink, M. (2004). Time reversal of electromagnetic waves. *Physical review letters*, 92(19), 193904.

- [67]Karami, H., Azadifar, M., Mostajabi, A., Rubinstein, M., & Rachidi, F. (2019). Numerical and experimental validation of electromagnetic time reversal for geolocation of lightning strikes. *IEEE Transactions on Electromagnetic Compatibility*, 62(5), 2156-2163.
- [68]Forest, M., & Hofer, W. J. (1992, June). TLM synthesis of microwave structures using time reversal. In *1992 IEEE MTT-S Microwave Symposium Digest* (pp. 779-782). IEEE.
- [69]Hofer, W. J. (2014). Computational time reversal—A frontier in electromagnetic structure synthesis and design. *IEEE Transactions on Microwave Theory and Techniques*, 63(1), 3-10.
- [70]Zhu, J. G., Jiang, Y., Stancil, D. D., & Moura, J. (2005, July). A novel time reversal method for target detection in cluttered media. In *2005 IEEE Antennas and Propagation Society International Symposium* (Vol. 4, pp. 135-138). IEEE.
- [71]Moura, J. M., Jin, Y., Stancil, D., Zhu, J. G., Cepni, A., Jiang, Y., & Henty, B. (2005, March). Single antenna time reversal adaptive interference cancellation. In *Proceedings (ICASSP'05). IEEE International Conference on Acoustics, Speech, and Signal Processing, 2005.* (Vol. 4, pp. iv-1121). IEEE.
- [72]Moura, J. M., Jin, Y., Stancil, D., Zhu, J. G., Cepni, A., Jiang, Y., & Henty, B. (2005, June). Time reversal adaptive interference cancellation and detection. In *the 13th Annual Workshop on Adaptive Sensor Array Processing*.
- [73]Cepni, A. G., Stancil, D. D., Zhu, J. G., & Jiang, Y. (2005, July). Experimental results on target detection in cluttered medium using electromagnetic time-reversal techniques. In *2005 IEEE Antennas and Propagation Society International Symposium* (Vol. 4, pp. 139-142). IEEE.
- [74]Moura, J. M., & Jin, Y. (2006). Detection by time reversal: Single antenna. *IEEE transactions on signal processing*, 55(1), 187-201.
- [75]Yavuz, M. E., & Teixeira, F. L. (2005). A numerical study of time-reversed UWB electromagnetic waves in continuous random media. *IEEE Antennas and Wireless Propagation Letters*, 4, 43-46.
- [76]Liu, D., Kang, G., Li, L., Chen, Y., Vasudevan, S., Joines, W., ... & Carin, L. (2005). Electromagnetic time-reversal imaging of a target in a cluttered environment. *IEEE transactions on antennas and propagation*, 53(9), 3058-3066.

- [77] Sarabandi, K., Koh, I., & Casciato, M. D. (2004, June). Demonstration of time reversal methods in a multi-path environment. In *IEEE Antennas and Propagation Society Symposium, 2004*. (Vol. 4, pp. 4436-4439). IEEE.
- [78] Emami, S. M., Hansen, J., Kim, A. D., Papanicolaou, G., Paulraj, A. J., Cheung, D., & Prettie, C. (2004). Predicted time reversal performance in wireless communications using channel measurements. *IEEE Communications Letters*, 2(2), 36-38.
- [79] Oestges, C., Hansen, J., Emami, S. M., Kim, A. D., Papanicolaou, G., & Paulraj, A. J. (2004, October). Time reversal techniques for broadband wireless communication systems. In *European Microwave Conference (Workshop)* (pp. 49-66).
- [80] Kyritsi, P., Papanicolaou, G., Eggers, P., & Oprea, A. (2004). MISO time reversal and delay-spread compression for FWA channels at 5 GHz. *IEEE Antennas and Wireless Propagation Letters*, 3(1), 96-99.
- [81] Fan, W., & Chen, Z. (2016, May). A condition for multiple source reconstructions with the time-reversal methods. In *2016 Ieee Mtt-S International Microwave Symposium (Ims)* (pp. 1-4). IEEE.
- [82] Fan, W., & Chen, Z. D. (2017, June). A new time reversal method with extended source locating capability. In *2017 IEEE MTT-S International Microwave Symposium (IMS)* (pp. 704-706). IEEE.
- [83] Fan, W., Chen, Z., & Hoefler, W. J. (2017). Source reconstruction from wideband and band-limited responses by FDTD time reversal and regularized least squares. *IEEE Transactions on Microwave Theory and Techniques*, 65(12), 4785-4793.
- [84] Liang, J. C., Chen, Z., Wang, J. F., Zhao, H. P., Peng, C., & Liu, Z. (2019, June). Time-reversal reconstructions of clustered sources and diagnosis of faulty antenna elements in three dimensions. In *2019 IEEE MTT-S International Microwave Symposium (IMS)* (pp. 114-116). IEEE.
- [85] Sadiku, M. N. (2001). *Numerical techniques in electromagnetics*. CRC press.
- [86] Hoefler, W. J. (2018). Time reversal in electromagnetics. *Wiley Encyclopedia of Electrical and Electronics Engineering*, 1-24.
- [87] Pendry, J. B. (2008). Time reversal and negative refraction. *Science*, 322(5898), 71-73.

- [88] De Rosny, J., Lerosey, G., & Fink, M. (2010). Theory of electromagnetic time-reversal mirrors. *IEEE Transactions on Antennas and Propagation*, 58(10), 3139-3149.
- [89] Ott, H. W. (2011). *Electromagnetic compatibility engineering*. John Wiley & Sons.
- [90] Wang, T., Qiu, S., Shi, L. H., & Li, Y. (2017). Broadband VHF localization of lightning radiation sources by EMTR. *IEEE Transactions on Electromagnetic Compatibility*, 59(6), 1949-1957.
- [91] Dardari, D., Closas, P., & Djurić, P. M. (2015). Indoor tracking: Theory, methods, and technologies. *IEEE Transactions on Vehicular Technology*, 64(4), 1263-1278.
- [92] Li, Q., Wang, Z., Xie, Y. Z., Rachidi, F., & Rubinstein, M. (2021). A correlation-based electromagnetic time reversal technique to locate indoor transient radiation sources. *IEEE Transactions on Microwave Theory and Techniques*, 69(9), 3945-3957.
- [93] Karami, H., Azadifar, M., Mostajabi, A., Favrat, P., Rubinstein, M., & Rachidi, F. (2020). Localization of electromagnetic interference sources using a time-reversal cavity. *IEEE Transactions on Industrial Electronics*, 68(1), 654-662.
- [94] Zhao, H., Tao, S., Chen, Z., & Hu, J. (2018). Sparse source model for prediction of radiations by transmission lines on a ground plane using a small number of near-field samples. *IEEE Antennas and Wireless Propagation Letters*, 18(1), 103-107.
- [95] Wang, L., Zhang, Y., Han, F., Zhou, J., & Liu, Q. H. (2020). A phaseless inverse source method (PISM) based on near-field scanning for radiation diagnosis and prediction of PCBs. *IEEE Transactions on Microwave Theory and Techniques*, 68(10), 4151-4160.
- [96] Zhang, J. C., Wei, X., Ding, L., Gao, X. K., & Xu, Z. X. (2020). An EM imaging method based on plane-wave spectrum and transmission line model. *IEEE Transactions on Microwave Theory and Techniques*, 68(10), 4161-4168.
- [97] Persson, K., Gustafsson, M., Kristensson, G., & Widenberg, B. (2013). Source reconstruction by far-field data for imaging of defects in frequency selective radomes. *IEEE Antennas and Wireless Propagation Letters*, 12, 480-483.
- [98] Persson, K., Gustafsson, M., Kristensson, G., & Widenberg, B. (2014). Radome diagnostics—Source reconstruction of phase objects with an equivalent currents approach. *IEEE Transactions on Antennas and Propagation*, 62(4), 2041-2051.

- [99] ©2022 IEEE. Feng, X. Y., Chen, Z., Xu, Z. M., & Li, J. (2022). Time-reversal source reconstruction with space and time kurtoses. *IEEE Transactions on Antennas and Propagation*, 70(6), 4766-4773.
- [100] Wu, H. S., & Barba, J. (1998). Minimum entropy restoration of star field images. *IEEE Transactions on Systems, Man, and Cybernetics, Part B (Cybernetics)*, 28(2), 227-231.
- [101] Xu, X., Miller, E. L., & Rappaport, C. M. (2003). Minimum entropy regularization in frequency-wavenumber migration to localize subsurface objects. *IEEE Transactions on Geoscience and Remote Sensing*, 41(8), 1804-1812.
- [102] Lopato, P., & Chady, T. (2012). Time reversal pulsed terahertz inspection of dielectric structures. *International Journal of Applied Electromagnetics and Mechanics*, 39(1-4), 427-433.
- [103] Mukherjee, S., Udpa, L., Udpa, S., & Rothwell, E. J. (2016). Target localization using microwave time-reversal mirror in reflection mode. *IEEE Transactions on Antennas and Propagation*, 65(2), 820-828.
- [104] ©2020 IEEE. Feng, X. Y., Chen, Z., & Liang, J. C. (2020, August). The entropy technique for the time-reversal source reconstruction. In *2020 IEEE/MTT-S International Microwave Symposium (IMS)* (pp. 158-160). IEEE.
- [105] ©2021 IEEE. Feng, X. Y., Chen, Z., & Xu, Z. M. (2021). Time-reversal source reconstruction with electromagnetic kurtosis. *IEEE Transactions on Antennas and Propagation*, 69(10), 6816-6823.
- [106] Westfall, P. H. (2014). Kurtosis as peakedness, 1905–2014. RIP. *The American Statistician*, 68(3), 191-195.
- [107] Moors, J. J. A. (1986). The meaning of kurtosis: Darlington reexamined. *The American Statistician*, 40(4), 283-284.
- [108] Balanda, K. P., & MacGillivray, H. L. (1988). Kurtosis: a critical review. *The American Statistician*, 42(2), 111-119.
- [109] Khan, M. G., Sallberg, B., Nordberg, J., & Claesson, I. (2009, September). Non-coherent detection of impulse radio UWB signals based on fourth order statistics. In *2009 IEEE International Conference on Ultra-Wideband* (pp. 824-828). IEEE.

- [110] Yang, A., Nie, H., Xu, Z., & Chen, Z. Modified kurtosis detection for impulse radio UWB signals. In *Proc. 2013 IEEE Radio and Wireless Symposium (RWS2013)* (pp. 136-138).
- [111] Jin, J. M. (2011). *Theory and computation of electromagnetic fields*. John Wiley & Sons.
- [112] Taflove, A., Umashankar, K. R., Beker, B., Harfoush, F., & Yee, K. S. (1988). Detailed FD-TD analysis of electromagnetic fields penetrating narrow slots and lapped joints in thick conducting screens. *IEEE Transactions on Antennas and Propagation*, 36(2), 247-257.
- [113] Karami, H., Azadifar, M., Wang, Z., Rubinstein, M., & Rachidi, F. (2021). Single-Sensor EMI Source Localization Using Time Reversal: An Experimental Validation. *Electronics*, 10(19), 2448.

APPENDIX A THE FDTD PROGRAMMING DETAILS

Table A.1 Correspondences between the components of (2.4) and those programmed in computers. I_{\max} , J_{\max} and K_{\max} denote the maximum ranges of the three-dimensional solution domain.

Original of (2.4)	Modified programming	Ranges of (i, j, k)
$H_x(x_i, y_{j+1/2}, z_{k+1/2}, t_{n+1/2})$	$H_x(i, j, k, n)$	$i = 1, \dots, I_{\max}-1$ $j = 0, \dots, J_{\max}-1$ $k = 0, \dots, K_{\max}-1$
$H_y(x_{i+1/2}, y_j, z_{k+1/2}, t_{n+1/2})$	$H_y(i, j, k, n)$	$i = 0, \dots, I_{\max}-1$ $j = 1, \dots, J_{\max}-1$ $k = 0, \dots, K_{\max}-1$
$H_z(x_{i+1/2}, y_{j+1/2}, z_k, t_{n+1/2})$	$H_z(i, j, k, n)$	$i = 0, \dots, I_{\max}-1$ $j = 0, \dots, J_{\max}-1$ $k = 1, \dots, K_{\max}-1$
$E_x(x_{i+1/2}, y_j, z_k, t_n)$	$E_x(i, j, k, n)$	$i = 0, \dots, I_{\max}-1$ $j = 1, \dots, J_{\max}-1$ $k = 1, \dots, K_{\max}-1$
$E_y(x_i, y_{j+1/2}, z_k, t_n)$	$E_y(i, j, k, n)$	$i = 1, \dots, I_{\max}-1$ $j = 0, \dots, J_{\max}-1$ $k = 1, \dots, K_{\max}-1$
$E_z(x_i, y_j, z_{k+1/2}, t_n)$	$E_z(i, j, k, n)$	$i = 1, \dots, I_{\max}-1$ $j = 1, \dots, J_{\max}-1$ $k = 0, \dots, K_{\max}-1$
$J_x(x_{i+1/2}, y_j, z_k, t_n)$	$J_x(i, j, k, n)$	$i = 0, \dots, I_{\max}-1$ $j = 1, \dots, J_{\max}-1$ $k = 1, \dots, K_{\max}-1$
$J_y(x_i, y_{j+1/2}, z_k, t_n)$	$J_y(i, j, k, n)$	$i = 1, \dots, I_{\max}-1$ $j = 0, \dots, J_{\max}-1$ $k = 1, \dots, K_{\max}-1$
$J_z(x_i, y_j, z_{k+1/2}, t_n)$	$J_z(i, j, k, n)$	$i = 1, \dots, I_{\max}-1$ $j = 1, \dots, J_{\max}-1$ $k = 0, \dots, K_{\max}-1$

With the above programming index notations, the FDTD equations are coded as follows:

$$H_x(i, j, k, n) = H_x(i, j, k, n-1) + \frac{\Delta t}{\mu \delta} \left[E_y(i, j, k+1, n) - E_y(i, j, k, n) + E_z(i, j, k, n) - E_z(i, j+1, k, n) \right], \quad (\text{A.1a})$$

$$H_y(i, j, k, n) = H_y(i, j, k, n-1) + \frac{\Delta t}{\mu \delta} \left[E_z(i+1, j, k, n) - E_z(i, j, k, n) + E_x(i, j, k, n) - E_x(i, j, k+1, n) \right], \quad (\text{A.1b})$$

$$H_z(i, j, k, n) = H_z(i, j, k, n-1) + \frac{\Delta t}{\mu \delta} \left[E_x(i, j+1, k, n) - E_x(i, j, k, n) + E_y(i, j, k, n) - E_y(i+1, j, k, n) \right], \quad (\text{A.1c})$$

$$E_x(i, j, k, n+1) = E_x(i, j, k, n) + \frac{\Delta t}{\epsilon \delta} \left[H_z(i, j, k, n) - H_z(i, j-1, k, n) + H_y(i, j, k-1, n) - H_y(i, j, k, n) - \delta J_x(i, j, k, n) \right], \quad (\text{A.1d})$$

$$E_y(i, j, k, n+1) = E_y(i, j, k, n) + \frac{\Delta t}{\epsilon \delta} \left[H_x(i, j, k, n) - H_x(i, j, k-1, n) + H_z(i-1, j, k, n) - H_z(i, j, k, n) - \delta J_y(i, j, k, n) \right], \quad (\text{A.1e})$$

$$E_z(i, j, k, n+1) = E_z(i, j, k, n) + \frac{\Delta t}{\epsilon \delta} \left[H_y(i, j, k, n) - H_y(i-1, j, k, n) + H_x(i, j-1, k, n) - H_x(i, j, k, n) - \delta J_z(i, j, k, n) \right]. \quad (\text{A.1f})$$

The spatial relationship of the field components in a unit cell of Yee's lattice is shown below:

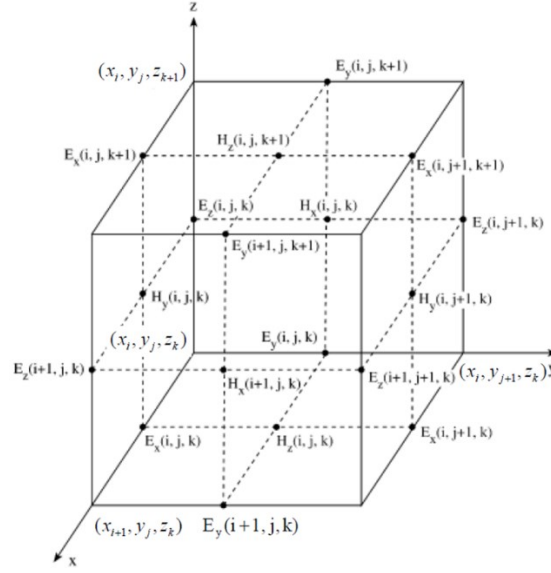


Figure A.1 The space configuration of electromagnetic fields in a typical unit cell.

For the boundary conditions of a cavity with PEC walls, normal components of magnetic field should be zero:

$$H_x(0, j, k, n) = H_x(I_{\max}, j, k, n) = 0, \quad (\text{A.2a})$$

$$H_y(i, 0, k, n) = H_y(i, J_{\max}, k, n) = 0, \quad (\text{A.2b})$$

$$H_z(i, j, 0, n) = H_z(i, j, K_{\max}, n) = 0; \quad (\text{A.2c})$$

and tangential components of electric field should be zero:

$$E_x(i, 0, k, n) = E_x(i, J_{\max}, k, n) = E_x(i, j, 0, n) = E_x(i, j, K_{\max}, n) = 0, \quad (\text{A.2d})$$

$$E_y(0, j, k, n) = E_y(I_{\max}, j, k, n) = E_y(i, j, 0, n) = E_y(i, j, K_{\max}, n) = 0, \quad (\text{A.2e})$$

$$E_z(i, 0, k, n) = E_z(i, J_{\max}, k, n) = E_z(0, j, k, n) = E_z(I_{\max}, j, k, n) = 0. \quad (\text{A.2f})$$

With all these notations, we code an in-house three-dimensional FDTD method and use it for our analysis and simulations. We also develop the one-dimensional and the two-dimensional FDTD codes by simply removing the second and the third dimensions of the above equations.

APPENDIX B MATHEMATICAL PROPERTIES OF ENTROPY

There are two main mathematical properties of entropy in this thesis:

First, entropy is related to field distribution but not affected by field intensity.

Imagine a new field distribution $E' = mE$, where m is a constant and $m \neq 0$. Then the entropy of the new field distribution is

$$\alpha'(n) = \frac{\left[\sum_i \sum_j \sum_k m^2 E^2(i, j, k, n) \right]^2}{\sum_i \sum_j \sum_k [mE(i, j, k, n)]^4} = \alpha(n), \quad (\text{B. 1})$$

which is equal to its original value.

Second, entropy has its upper and lower limits according to a specific solution domain.

Suppose the total number of cells in the space is L , then we have

$$1 \leq \alpha \leq L. \quad (\text{B. 2})$$

The proof in detail is shown below:

Let us first define $W(l, n) = E^2(i, j, k, n)$, where $l = 1, 2, \dots, L$ refers to all spatial nodes; thus $W \geq 0$. Considering the entropy value at any time step n , and rewriting $W(l, n)$ as W_l , entropy can be written as

$$\alpha = \left(\sum_{l=1}^L W_l \right)^2 / \sum_{l=1}^L W_l^2. \quad (\text{B. 3})$$

First, we consider the left-hand side. It is clear that

$$\alpha = \frac{\sum_{l=1}^L W_l^2 + \sum_{\substack{l,m=1 \\ l \neq m}}^L W_l W_m}{\sum_{l=1}^L W_l^2} = 1 + \frac{\sum_{\substack{l,m=1 \\ l \neq m}}^L W_l W_m}{\sum_{l=1}^L W_l^2} \geq 1. \quad (\text{B. 4})$$

The lower limit can be achieved only when one node has non-zero field value.

Then we use the mathematical induction method to prove the right-hand side:

a) If $L = 2$, it is clear that $\alpha = \frac{(W_1 + W_2)^2}{W_1^2 + W_2^2} \leq 2$; only when $W_1 = W_2$, $\alpha = 2$.

b) If $L = m$ ($m \geq 2$), suppose we have $\alpha = \left(\sum_{l=1}^m W_l \right)^2 / \sum_{l=1}^m W_l^2 \leq m$, that is

$$\left(\sum_{l=1}^m W_l \right)^2 \leq m \sum_{l=1}^m W_l^2. \quad (\text{B. 5})$$

From (B. 5), we can have

$$\left(\sum_{l=1}^m W_l \right)^2 \leq m \sum_{l=1}^m W_l^2 + \sum_{l=1}^m (W_l - W_{m+1})^2. \quad (\text{B. 6})$$

Rewriting (B. 6), we have

$$\left(\sum_{l=1}^m W_l \right)^2 + 2W_{m+1} \sum_{l=1}^m W_l + W_{m+1}^2 \leq (m+1) \sum_{l=1}^{m+1} W_l^2. \quad (\text{B. 7})$$

That is

$$\left(\sum_{l=1}^{m+1} W_l \right)^2 / \sum_{l=1}^{m+1} W_l^2 \leq m+1. \quad (\text{B. 8})$$

Only when $W_1 = W_2 = \cdots = W_{m+1}$, (B. 8) equals $m+1$.

According to (B. 8), we prove the right-hand side for the situation of $L = m + 1$ from (B. 5).

To sum up, we have proved $\alpha \leq L$.